LUND UNIVERSITY
Faculty of Science

Identification of Neutrons Using Digitized Waveforms

Rasmus Kjær Høier

Thesis submitted for the degree of Master of Science
Project duration: 18 months, 60 hp

Supervised by Kevin Fissum and Hanno Perrey

Department of Physics
Division of Nuclear Physics
May, 2019

Abstract

The advantages of performing neutron-tagging measurements using a waveform digitizer are explored. An existing analog setup consisting of modular crate electronics at the Source-Testing Facility at the Division of Nuclear Physics in Lund, Sweden has been digitally replicated. Neutrons are detected using an organic liquid-scintillator detector while the corresponding 4.44 MeV gamma-rays are detected using inorganic scintillation crystals. The performance of the digitizer-based setup is compared to that of the modular analog setup in terms of neutron and gamma-ray pulse-shape discrimination and time-of-flight. The results obtained using the digitizer-based approach are superior to those obtained using the modular analog approach in all aspects. The digitizer-based approach is then successfully employed both to distinguish between neutrons and gamma-rays via a convolutional neural network and to relate neutron deposition energy to neutron kinetic energy via time-of-flight.

Acknowledgments

I would like to thank all the members of the Sonnig group for creating a friendly atmosphere and providing helpful feedback. In particular I want to thank my supervisors Hanno and Kevin. You gave me the freedom to jump down rabbit holes and open up cans of worms, but always helped me to stay on track. I very much appreciate your guidance and support throughout this project. Finally I want to thank my wife Cibele. This project would not have been possible without your patience and advice.

Contents

List of Figures

List of Tables

List of Abbreviations

CC Charge Comparison
CFD Constant-Fraction Discriminator
CNN Convolutional Neural Network
DAQ Data Acquisition
ESS European Spallation Source
FIFO Fan-In Fan-Out
FoM Figure-of-Merit
LG Long gate
NIM Nuclear Instrument Module
PMT Photomultiplier Tube
PS Pulse Shape
PSD Pulse-Shape Discrimination
QDC Charge-to-Digital Converter
SG Short gate
STF Source-Testing Facility
TDC Time-to-Digital Converter
ToF Time-of-Flight
VME Versa Module Europa

Chapter 1

Introduction

1.1 Motivation

In the late 1960s, the Nuclear Instrument Module (NIM) standard for experimental physics electronics was established. The NIM standard specifies certain parameters, such as module dimensions and back-plane voltages, which make it possible to easily combine electronics modules from different manufacturers into a single signal-processing system. These modules each perform specific tasks, such as enforce thresholds, copy or sum signals or perform logic operations. When combined, they can be used to process signals from experiments in the analog domain. The modular design also makes it easy to assemble, disassemble and recombine the modules to perform a wide array of different signal processing tasks. This makes it possible to easily construct electronics for signal processing in nuclear-physics experiments without necessarily knowing all of the exact functional parameters of each component. Simply knowing the operation the component is to perform is sufficient. Later, additional modularized electronics components which allow for an interface to computers were introduced. For example, the Versa Module Europa (VME) modules are a widely used format for digitizing various features of analog input signals, such as charge or time differences. VME modules can be considered a bridge between the analog and digital domains.

Today, a leap forward is being taken in the field of instrumentation electronics with the adoption of fully digital signal-processing techniques. This step is possible due to a variety of factors. For example, storage prices of less than 0.5 SEK per GB make it feasible to save much more information than ever before. Also, increases in computer processing power have made the detailed investigation of large data sets more practical. Further, the falling cost and increasing performance of digitizers, devices which digitally sample analog signals at up to GHz frequencies, is key. We are now positioned on the cusp of the truly digital domain.

Currently, a wide variety of detectors under development for the European Spallation Source (ESS) need to be characterized. In particular, the ^{3}He crisis has made it necessary to invent new detector technologies with high pixel count and granularity. The Source-Testing Facility (STF) at the Division of Nuclear Physics in Lund, Sweden, cur-

rently provides well-understood radioactive sources and a dedicated experimental setup for detector characterization. The setup is quasi-digital employing various standard NIM modules for analog signal processing with digitization of charge and timing information performed by VME modules. Although this setup does employ some digitization, it will be referred to as the analog setup to distinguish it from a fully digitizer-based digital setup. Using the analog setup, most components must be painstakingly fine tuned for a particular detector setup by changing delays, gate lengths and thresholds in order to optimize the performance. This is not a trivial task.

The motivation for the work performed in this thesis is to emulate the NIM/VME based detector-characterization data-acquisition setup currently employed at the STF with a fully digital digitizer-based system. In doing so, a large number of NIM and VME modules which need to be individually tuned to the task at hand will be replaced by a single digitizer module. This will enable optimizations to be performed digitally and make it possible to study the effects of various thresholds, delays and gate lengths on the same data set offline. Furthermore, access to the digitized waveforms on a pulse-by-pulse basis will make it possible for advanced pulse-shape discrimination (PSD) techniques to be applied to the data.

Thus, the potential of using modern digitization techniques to complement an existing analog setup will be evaluated by comparing the performance of a well-established analog setup with that of a digitizer-based setup. A classical charge-comparison method will be employed for analog/digital PSD benchmarking. Furthermore, fully digital PSD will be investigated using a convolutional neural network, a technique which is not available when employing an analog electronics setup.

1.2 The Basics

1.2.1 Neutron/Matter Interactions

Neutrons are subatomic particles which together with protons make up atomic nuclei. With a mass of $939.6\,\mathrm{MeV}/c^2$, the neutron is $1.293\,\mathrm{MeV}/c^2$ more massive than the proton and 1839 times as massive as the electron. Free neutrons were first discovered by Chadwick in 1932, and have since come to play an important role as probes of matter. This is due to the fact that they are uncharged particles. With zero net electric charge, neutrons are a relatively penetrating type of radiation, capable of moving through the electric fields of charged particles unaffected. When not bound in a nucleus, a neutron decays into a proton via beta decay. This process has a half-life of 10.2 minutes [1], which means that neutrons have to be freed from nuclei at the location of the experiment that will use them.

Neutrons are often classified according to their energy, since in different energy ranges, they have different probabilities for interactions of different types. The classifications shown in Table 1.1 are given by Krane [2]. Fast neutrons are of particular interest to this project. For fast neutrons, the dominating interactions with matter are elastic and inelastic scattering. In elastic scattering, the neutron generally transfers part of its

Name	Energy
thermal	0.025 eV
epithermal	1 eV
slow	1 keV
fast	0.1-10 MeV

Table 1.1: Neutron nomenclature as a function of energy.

kinetic energy to a nucleus which recoils from the collision in its ground state. In inelastic scattering, the recoiling nucleus is excited, and it later de-excites by emitting for example a gamma-ray. Thermal neutrons have wavelengths on the order of 0.1 nm which makes them useful for examining the structure of matter on an atomic scale. Thermal neutrons interact predominantly via absorption. Here a nucleus absorbs a neutron resulting in a different isotope of the same element, usually in an excited state. De-excitation can occur via the emission of for example a gamma-ray [3]. The probability for neutron absorption is roughly inversely proportional to its velocity. This means that fast neutrons need to first be slowed down or moderated to thermal energies if they are to undergo neutron absorption.

1.2.2 Sources of Free Neutrons

Free neutrons can be produced for experimental use in different ways. Large-scale production involves accelerator facilities or nuclear reactors. Spallation neutron sources such as ESS will produce neutrons by directing a highly energetic beam of protons onto a neutron-rich target. The collision will cause the target nucleus to fragment in a process known as spallation releasing many neutrons. For example, in the case of a single GeV proton hitting a lead nucleus, around 25 neutrons may be produced [4]. Spallation neutron sources produce higher instantaneous neutron rates than any other currently existing man-made neutron source. Nuclear reactors produce large fluxes of neutrons through fission, and a neutron beamline can be created by constructing a penetration in the shielding [2]. The fundamental difference between an accelerator-based neutron beam and a reactor-based neutron beam is that the former is pulsed whereas the latter is continuous. In either case, with moderation and specialized instruments, neutron beams with specific energies can be produced.

On a smaller scale, neutrons may be freed by radioactive sources. An actinide-Beryllium neutron source is a combination of an alpha particle emitting actinide and a Beryllium base. For example, the actinide ^{238}Pu decays into ^{234}U as follows:

$$\begin{aligned} {}^{238}\mathrm{Pu} &\rightarrow {}^{234}\mathrm{U}' + \alpha\,(Q_1 - \textstyle\sum_i E_{\gamma_i}) \\ &\rightarrow {}^{234}\mathrm{U} + \alpha(Q_1). \end{aligned} \tag{1.1}$$

The reaction has a Q-value Q_1=5.59 MeV, which is energy shared between the recoil nucleus and the alpha particle. Note that the ^{234}U nucleus may be left in either an

excited state or in its ground state. If it is left in its ground state, then the alpha particle can at most receive a kinetic energy of Q_1. If instead the nucleus recoils in an excited state (labeled $^{234}\mathrm{U}'$ above), then less energy will be available for the alpha particle. Depending upon the excited state, one or multiple gamma-rays may be released as the recoiling $^{234}\mathrm{U}$ de-excites. This cascade of gamma-rays is useful, see Sec. 1.2.5.

Subsequent to its production, the alpha particle may then strike a $^{9}\mathrm{Be}$ nucleus, producing $^{12}\mathrm{C}$ and a free neutron, as shown below:

$$\begin{aligned} \alpha(Q_1) \; + \; {}^{9}\mathrm{Be} \; &\rightarrow \; {}^{12}\mathrm{C} \; + \; n(Q_1+Q_2) && 35\% \\ &\rightarrow \; {}^{12}\mathrm{C}^{*} \; + \; n(Q_1+Q_2-E_1) && 55\% \\ &\rightarrow \; {}^{12}\mathrm{C}^{**} \; + \; n(Q_1+Q_2-E_2) && 15\%. \end{aligned} \tag{1.2}$$

This reaction has a Q-value of Q_2=5.70 MeV, which is shared between the recoiling carbon nucleus and the neutron according to momentum conservation. Roughly 35% of the time, $^{12}\mathrm{C}$ is produced in its ground state and the neutron can at most obtain energy Q_1+Q_2=11.29 MeV. Approximately 55% of the time, $^{12}\mathrm{C}$ recoils in its first excited state and de-excites by emitting a 4.44 MeV gamma-ray. Thus, in the case of a neutron freed together with the production of $^{12}\mathrm{C}$ in its first excited state, the kinetic energy of the neutron will be limited to $Q_1+Q_2-E_\gamma = 6.85\,\mathrm{MeV}$. The gamma-ray emitted by the de-exciting $^{12}\mathrm{C}$ is useful, see Sec. 1.2.5. Around 15% of the time, $^{12}\mathrm{C}$ recoils in the second excited state [5].

1.2.3 Scintillation Detectors

Scintillators generate pulses of visible light when ionizing radiation interacts with them. They are particularly useful for detecting uncharged particles such as gamma-rays and neutrons. An important feature of scintillators is that they should not re-absorb the scintillation light they themselves produce. This may be achieved by doping the scintillator, to facilitate de-excitations via different metastable states. The light emitted from the metastable states is shifted in energy so that it can pass through the scintillator without re-absorption. The lifetime of different metastable states may be exploited to identify the incident particle species, see Sec. 1.2.4.

Detecting Gamma-rays

Photons of different energies generate scintillation light through different interactions with atomic electrons. These interactions are the photoelectric effect, Compton scattering and pair production [2]. Photons of energies below 0.1 MeV generally interact with atomic electrons via the photo-electric effect. In this process, the photon is absorbed by a bound electron which is ejected from the atom with an energy equal to the difference between photon energy and the binding energy of the electron. This electron continues to interact in the detector. Compton scattering is the dominating effect between 0.1 and 5 MeV.

Here, a gamma-ray is scattered by a bound electron, which in turn is excited or freed from the atom. The scattered photon, which has been degraded in energy, continues to interact in the scintillator as does the recoiling electron. Pair production dominates beyond 5 MeV. Here, a gamma-ray of energy $E_\gamma > 2m_e$ spontaneously converts into an electron and a positron near a nucleus [2]. The electron and positron share any excess energy, which is then deposited in the scintillator via continued interactions. When the positron comes to rest, it annihilates with another electron resulting in two 0.511 MeV gamma-rays. These gamma-rays may continue to interact with the scintillator. They may even escape the detector.

Detecting Neutrons

For fast neutrons, scintillation light is mainly produced by charged recoils resulting from elastic scattering. In this case, the neutron energy will decrease from E to E' according to:

$$E' = E\left(1 - \frac{4m_A m_n \cos^2\theta}{(m_A + m_n)^2}\right), \tag{1.3}$$

where m_n and m_A are the neutron and nucleus masses and θ is the angle between the recoiling nucleus and the initial path of the neutron. From Eq. 1.3, it can be seen that neutrons generally give up a larger fraction of their energy when they scatter from lighter nuclei. For this reason, scintillation detectors are typically ^{1}H rich. The recoiling proton will then produce ionization in the scintillator as it deposits its energy, resulting in scintillation light.

Photomultiplier Tubes

A photomultiplier tube is a device used to convert scintillation photons into a current pulse, see Fig. 1.1. The scintillation light produced by neutrons and gamma-rays in a scintillator is converted to electrons at the photocathode via the photoelectric effect. The charge produced in this manner is not sufficient to result in a particularly strong signal, so a photomultiplier tube is used to increase the total charge. This results in a current pulse that is large enough to be processed.

The PMT is connected to a high voltage source which provides a potential difference between the photocathode and the anode. This potential difference is used to accelerate the electrons towards the anode through a series of dynodes. Each time an electron strikes a dynode, multiplication occurs. The magnitude of the multiplication depends on the gain and the number of dynodes, but factors of more than 10^7 are achievable. The advantage of a PMT is that it makes it possible to amplify charges by several orders of magnitude and that information about the original scintillation photon count and timing is preserved because the amplification is linear [3].

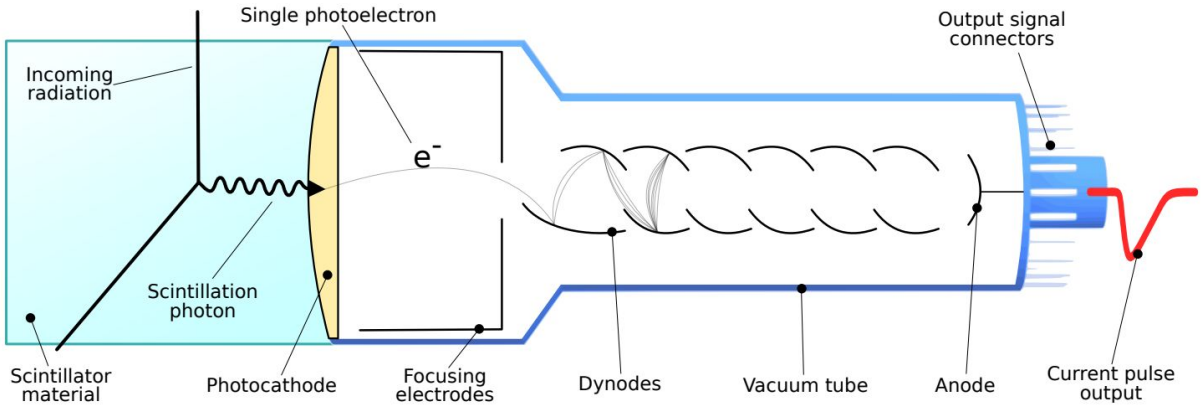

Figure 1.1: Scintillation detector. The blue volume to the left is the scintillator, which is coupled to a PMT via a photocathode (yellow). The grey curves represent the trajectories of the electrons and the black curves are the dynodes. The red pulse to the right is the resulting elecronic signal. Figure from Ref. [6].

1.2.4 Neutron/Gamma-Ray Discrimination

The metastable states of scintillators have associated average decay times. Furthermore, the probability of a metastable state being occupied depends on whether the incident particle is a gamma-ray or a neutron [2]. For some scintillators, the differences in decay times between different metastable states which are excited by different types of particle species are large. This means that the signals produced by neutrons (recoiling protons) and gamma-rays (recoiling electrons) have different time dependencies or shapes. This in turn makes it possible to discriminate between them based on the resulting pulse shape (PS). A scintillator which demonstrates PS sensitivity to different particle species is said to have pulse-shape discrimination (PSD) capabilities.

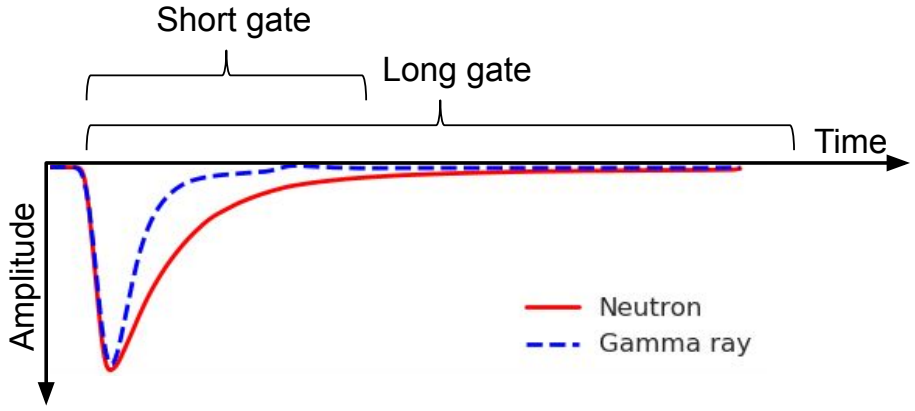

Figure 1.2: PS sensitivity. Typical shapes of neutron and gamma-ray pulses from a detector with PSD capabilities. The blue gamma-ray pulse is significantly shorter than the red neutron pulse. "Short gate" and "long gate" refer to integration times.

PS can be parameterized in many different ways. One common method is the charge comparison (CC) method. Pulses are integrated over two different timescales, typically referred to as "long gate" (LG) and "short gate" (SG). Typical neutron and gamma-ray pulse shapes are illustrated in Fig. 1.2 along with corresponding LG and SG integration windows. PS may be parameterized as:

$$\text{PS} \;=\; 1 - \frac{Q_{SG} + a}{Q_{LG} + b}, \tag{1.4}$$

where Q_{SG} and Q_{LG} are the total integrated charges in the SG and LG integration windows, respectively while a and b are constants added to the charge integrals Q_{LG} and Q_{SG} in order to facilitate fine tuning of the energy dependence of the PS parameter. With optimal choices of a and b, the neutron and gamma-ray distributions can be linearized, such that they can be separated with a single cut on the PS parameter, see Fig. 1.3.

If a scintillator has PSD capabilities, then signals from recoiling protons will have significantly more slow scintillation components. This will result in more charge in the tail of the scintillation pulse and hence a larger PS value than for electrons/gamma-rays. A typical way of visualizing the PS as a function of deposited energy is shown in Fig. 1.3. The upper distribution corresponds to neutrons and the lower corresponds to gamma-rays. It will generally be harder to discriminate between the two distributions at lower deposited energies.

A drawback with using analog electronics is that the LG and SG integration windows need to be decided before any measurements are taken. This makes optimization of the gate lengths tedious and time consuming, as an incorrect choice of gate length may render a data set useless. It is anticipated that the digitizer-based approach will greatly streamline this process, as gates can be optimized after the data have been collected.

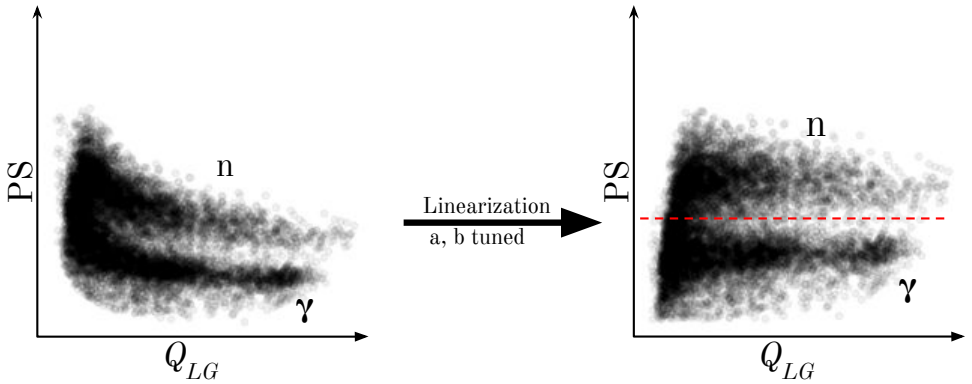

Figure 1.3: PS versus Q_{LG}. Left panel: the parameters a and b are both zero. Right panel: a and b have been tuned to achieve a linear separation between neutrons (upper band) and gamma-rays (lower band). A typical cut is marked with a dashed red line.

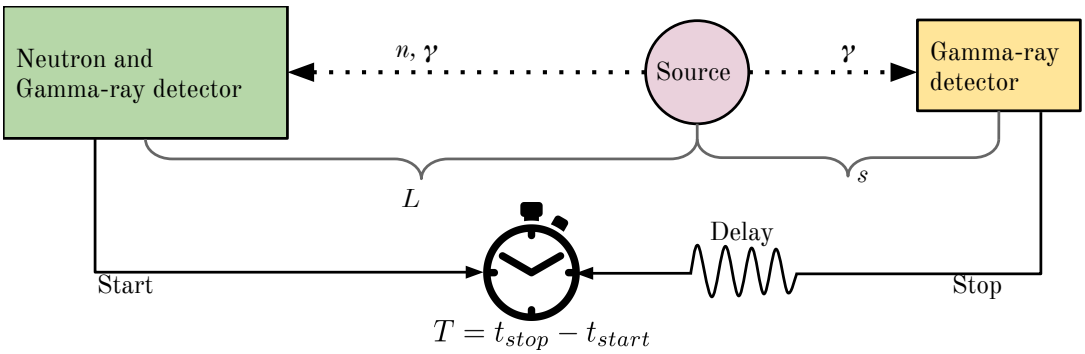

Figure 1.4: Illustration of the neutron-tagging setup. The detector sensitive to both neutrons and gamma-rays (green) is placed a distance L from the source (green). The gamma-ray detector (yellow) is placed closer to the source at a distance s.

1.2.5 Neutron Time-of-Flight and Tagging

Time-of-flight (ToF) measurements offer a conceptually elegant way to determine the energy of a particle based on a known distance and the corresponding flight time. The flight time is generally measured using a start pulse and a stop pulse together with a precision oscillator.

Recall that an actinide/Beryllium source produces neutrons and gamma-rays. The gamma-rays come both from the de-excitation of the actinide (a cascade of low-energy gamma-rays) which follow the alpha particle emission and from the de-excitation of the ^{12}C (a single 4.44 MeV gamma-ray). This single gamma-ray emitted in conjunction with the neutron may be used to "tag" the neutron and either start or stop a ToF measurement. Further, the low-energy gamma-ray cascade may be used to calibrate the ToF measurements.

By placing a gamma-ray detector close to the actinide/Beryllium source and a neutron /gamma-ray detector further away, the time difference between any two particles detected in the two detectors may be measured, see Fig. 1.4. Often signal delay will be applied to the gamma-ray detector to let the neutron/gamma-ray detector provide the start signal even though it is located further away from the source than the gamma-ray detector. In Fig. 1.4, the distance from the center of the actinide/Beryllium source to the center of the neutron/gamma-ray detector is L. Due to the applied delay the measured flight time T will be shorter for neutrons than for gamma-rays. By instead using

$$T' = -T, \tag{1.5}$$

time ordering is restored, with neutrons having longer flight times than gamma-rays. Figure 1.5 (left panel) shows a histogram of uncalibrated flight times T'. This spectrum may be calibrated by considering two coincidental low-energy cascade gamma-rays from the de-excitation of the actinide. One of these gamma-rays is detected by the neutron and gamma-ray sensitive detector, while the other is detected by the gamma-ray detector. Since the speed of the gamma-rays is c and the source-to-detector distances and delays are

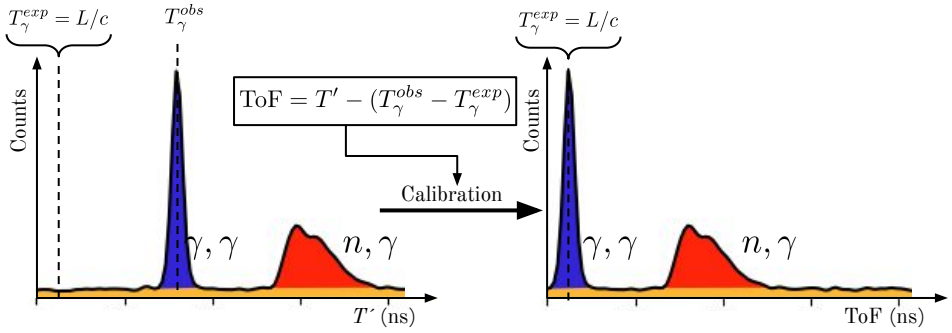

Figure 1.5: Sketch of a time-of-flight spectrum. Left: Spectrum of uncalibrated flight times. The gamma-flash is shaded blue, the neutron bump is shaded red, and the random coincidences are shaded orange. Right: The spectrum has been calibrated to a ToF spectrum by shifting T_γ^{obs} to T_γ^{exp}.

fixed, the time difference between the start and stop signals is also fixed. This constant time difference is known as the gamma-flash, and serves as an absolute timing calibration point for the flight-time measurement. This calibration may be carried out by shifting the observed location of the gamma-flash T_γ^{obs} to the expected location T_γ^{exp} defined as L/c. The calibrated time-of-flight, ToF is given by:

$$\mathrm{ToF} = T' - (T_\gamma^{obs} - T_\gamma^{exp}). \tag{1.6}$$

This produces the calibrated ToF spectrum shown in the right panel of Fig. 1.5. If instead a neutron is detected by the neutron and gamma-ray sensitive detector and a 4.44 MeV gamma-ray is detected by the gamma-ray detector, the flight time will always be longer than for a pair of gamma-rays because the speed of the neutron will always be less than c. From the resulting ToF for the neutron, the kinetic energy K_n may be determined classically according to:

$$K_n = \frac{1}{2} m_n v_n^2 = \frac{1}{2} m_n \left(\frac{L}{\mathrm{ToF}} \right)^2, \tag{1.7}$$

where m_n and v_n are the mass and the speed of the neutron, respectively. Thus knowledge of the distance from the center of the actinide/Beryllium source to the center of the neutron/gamma-ray detector together with the location of T_γ^{obs} in the uncalibrated flight-time spectrum is all that is needed to determine the energy of a tagged neutron on an event-by-event basis.

Figure 1.6 shows an example of a tagged neutron energy spectrum (grey) contrasted with the entire neutron energy spectrum (red) measured for a Pu/Be source [7]. In forming this spectrum the mapping from neutron ToF to neutron kinetic energy presented in Eq 1.7 has been applied. Although neutrons from a Pu/Be source can have up to ∼11 MeV, the tagged-neutron spectrum ends at ∼6.5 MeV. This is because only the neutrons accompanied by a 4.44 MeV gamma-ray are tagged. The full Pu/Be neutron

energy spectrum contains four peaks, two of which are visible in the tagged neutron spectrum. The reason that the full spectrum does not extend to as low energies as the tagged neutron spectrum may be that the tagged spectrum has employed a lower amplitude threshold.

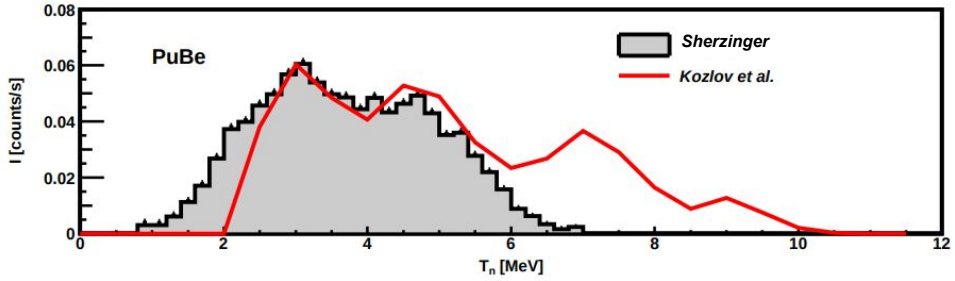

Figure 1.6: Reference neutron energy spectrum for a Pu/Be source. Grey: a tagged neutron energy spectrum. Red: Neutron energy spectrum. Figure from Scherzinger et al [7].

Chapter 2

Method

2.1 Experimental Infrastructure

2.1.1 Source-Testing Facility

The Source-Testing Facility (STF) at the Division of Nuclear Physics in Lund, Sweden, is a fully equipped user facility for the characterization of detectors, shielding and sources [8]. The operation of the STF is a collaborative effort between the Division of Nuclear Physics and the ESS Detector Group. It is employed for the development of detectors for ESS and industry. The STF offers easy and reliable access to actinide/Be fast-neutron sources and gamma-ray sources. Additionally, fast neutrons can be moderated to lower energies with various materials. The STF is divided into two areas, see Fig. 2.1. The user area contains data-acquisition systems (DAQs), workstations as well as a wide range of electronics modules and detectors. The smaller interlocked area is where measurements are carried out. This area contains an array of shielding materials as well as a dedicated neutron-tagging setup based upon the Aquarium.

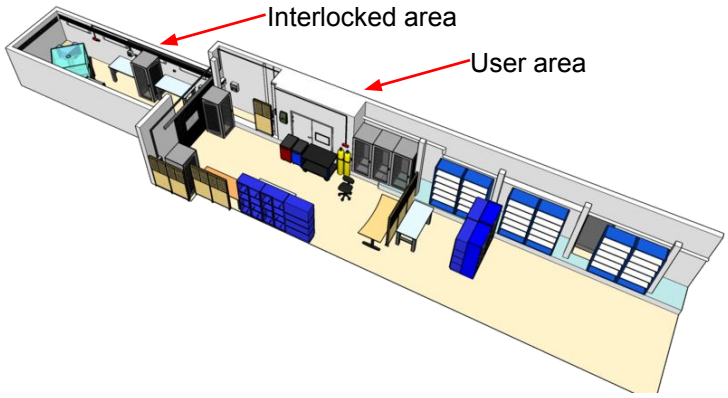

Figure 2.1: The Source-Testing Facility. The smaller room to the left is the interlocked area where measurements are carried out. The user area to the right contains DAQ setups, workstations and storage. Figure from Ref. [8].

2.1.2 The Aquarium

The fast-neutron source may be located inside a $140\times140\times140$ cm^3 tank of water referred to as the Aquarium, see Fig. 2.2. The Aquarium has four horizontal cylindrical beam ports intersecting at a central volume. A source and up to four gamma-ray detectors may be placed within the central volume. The beam ports are air filled, allowing neutrons and gamma-rays to reach a neutron/gamma-ray detector placed next to the aquarium without passing through shielding. Each of the beam ports can be plugged when not in use. By moderating and absorbing the fast neutrons, the water tank both provides shielding from the sources and gives rise to a distinguishable gamma-ray energy of 2.23 MeV produced in the de-excitation of the deuteron via the ^{1}H$(n,\gamma)^2$H* reaction. This gamma-ray is useful when performing energy calibrations, see Sec. 2.2.1 and Sec. 2.2.2. An actinide/Be source may be positioned on the central vertical axis of the Aquarium and can be raised to the same height as the ports for ToF measurements. In a "lowered" or "parked" position, there is no direct line-of-sight through air from the source through the ports. The four dedicated gamma-ray detectors are located near the source, but are raised slightly to allow a direct line-of-sight from source through the ports, see Fig. 2.2.

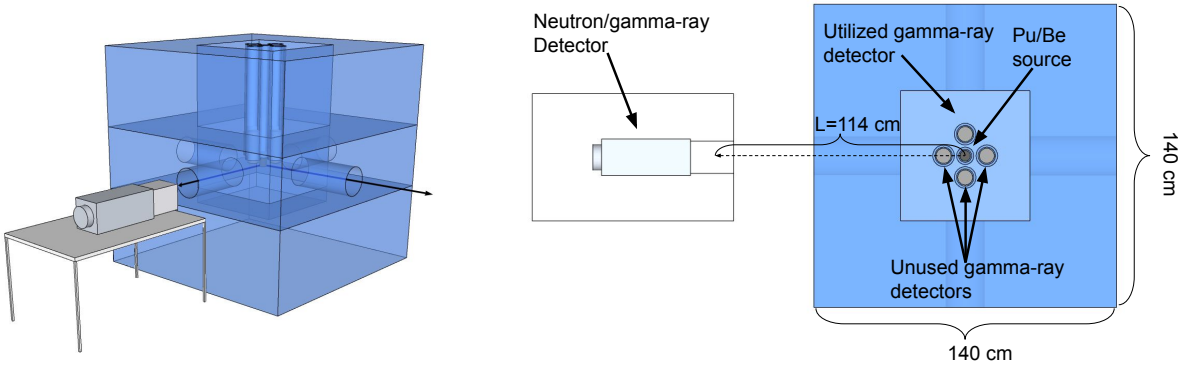

Figure 2.2: The Aquarium. Left panel: Oblique view with the neutron/gamma-ray detector in front of one of the horizontal cylindrical beam ports. Lines-of-sight from the source out of two of the ports are indicated with arrows. The source and the four gamma-ray detectors are located in the tubes at the center of the aquarium. Right panel: Top view with the source and detectors indicated by arrows.

2.1.3 Radiation Sources

Two radiation sources were used in this work. The actinide/Be fast-neutron and gamma-ray source ^{238}Pu/^{9}Be (referred to as Pu/Be) was used for tagging fast neutrons and for energy calibration of the neutron/gamma-ray detector. As shown in Sec. 1.2.2, the Pu/Be source produces both a cascade of low-energy photons and fast neutrons, which $\sim$55% of the time are accompanied by the emission of a 4.44 MeV gamma-ray. The source has been measured to produce approximately $2.99\cdot10^6$ neutrons per second [9]. The pure gamma-ray source ^{60}Co was used for detector calibration. ^{60}Co decays to excited states of

^{60}Ni via beta decay. De-excitation of ^{60}Ni will result in gamma-rays of energies 1.17 MeV or 1.33 MeV [1].

2.1.4 Fast-Neutron and Gamma-Ray Detectors

As ToF depends on the accurate timing of γn and $\gamma\gamma$ pairs, it is essential to detect both particle species with accurate timing. In this work, two different detectors were used for detecting neutrons and gamma-rays from the sources. Both of which produce pulses with negative polarity. A liquid organic NE213 detector was used to detect both gamma-rays and neutrons while an inorganic Cerium-doped Yttrium Aluminum Perovskite crystal (YAP) detector was used to detect gamma-rays.

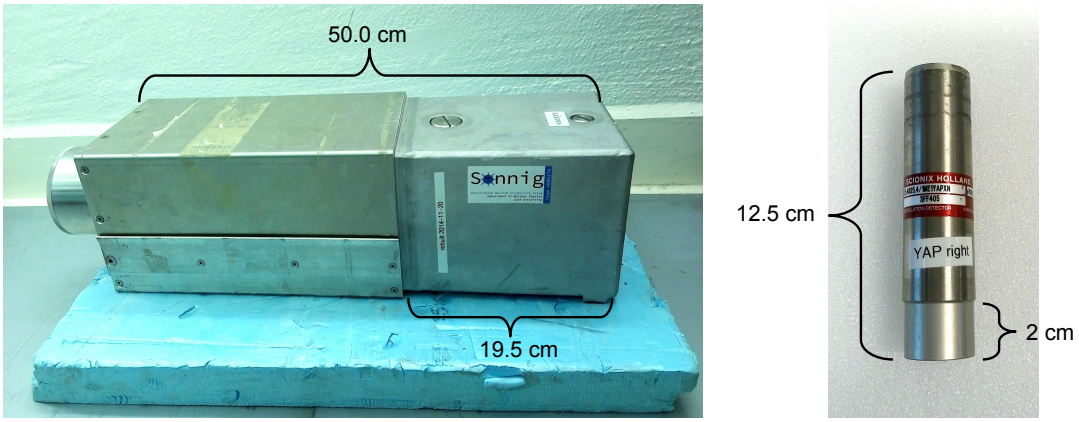

Figure 2.3: Photographs of the detectors. Left: NE213 detector. Right: YAP detector.

Since its introduction in the early 1960s, the NE213 liquid organic scintillator has become the gold standard for fast-neutron detection due to its excellent neutron/gamma-ray discrimination capabilities and high detection efficiency. The drawbacks of this scintillator are that it is toxic and highly volatile with a flash point of 26°C. The NE213 used here was produced by Nuclear Enterprises. It is equivalent to EJ301, currently produced by Eljen Technology [10]. The decay times of the first three scintillation components are 3.16 ns, 32.3 ns and 270 ns [10]. It is contained in a 122×122×179 mm^3 volume which is connected to a photomultiplier tube via a lightguide[1].

Near the source, four YAP detectors are placed. The YAP detectors are mounted on photomultiplier tubes. These inorganic scintillators are largely insensitive to neutrons and provide excellent timing of gamma-rays. As the YAP detectors are located closer to the source they experience a significantly higher gamma-ray flux than the NE213 detector does. This makes time resolution and decay time critical factors in their performance. The scintillation light has a decay time of ∼27 ns [12]. Howevever, it takes ∼100 ns for signals to return to the original baseline level. This means that the detector can handle count rates in the low MHz range without significant pileup. To simplify the analysis and limit the data rates, only one YAP detector was used in this project.

[1]This detector was constructed by Johan Sjögren as part of his thesis work in 2009-2010 [11].

2.2 Signal Processing

Two different experimental systems were employed. These experimental setups differed only in the DAQ system used and shared the same physical setup of detectors, shielding and radiation source. By sending the detector signals through an active splitter, both DAQs could be run in parallel on the exact same detector signals. The first setup employed NIM modules to process signals and generate a trigger decision. VME modules were used to digitize the timing and charge characteristics of the signals. The digitized data were transferred to a computer where they were saved and plotted in real time. Since this setup did most of the data processing via analog electronics, it will be referred to as the analog setup. The second setup was based on a digitizer which recorded detector signals as digital waveforms for offline analysis. Since all of the processing of the signals was performed digitally, this setup will be referred to as the digital setup. Figure 2.5 contrasts the analog and digital setups. The analog setup is composed of a variety of NIM and VME modules as well as a large number of LEMO cables. The digital setup is composed of a single digitizer, which fits in a single VME slot. The digital setup is thus far more compact spatially.

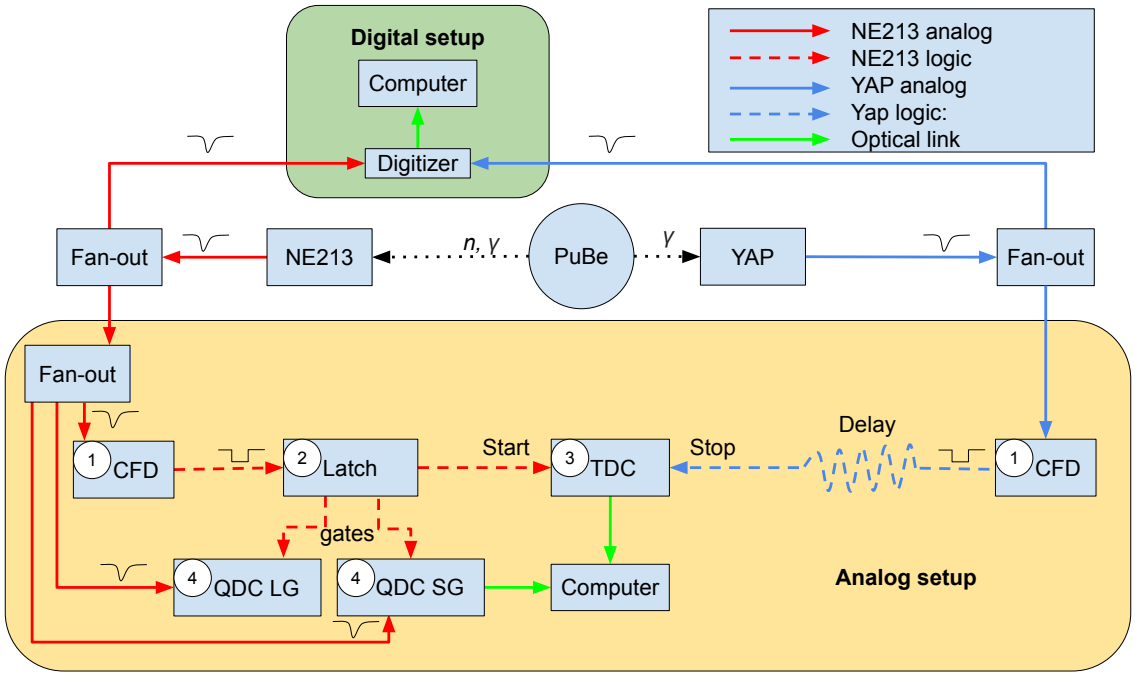

Figure 2.4: Schematic of the experimental setup. Green box: the digital setup. Yellow box: the analog setup.

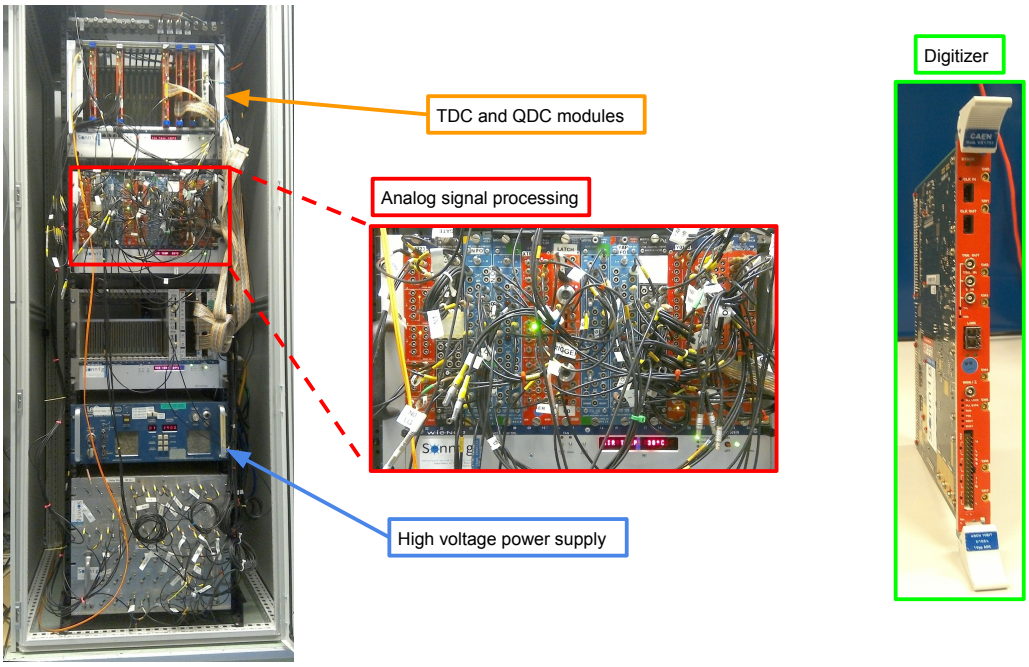

Figure 2.5: Data-acquisition systems. The analog DAQ rack is shown to the left. Digitization modules are highlighted by the orange arrow, and the power supply is indicated by the blue arrow. A closeup of the analog electronics is shown in the red box. The single digitizer module is shown highlighted in green to the right.

2.2.1 Analog

The detector signals were replicated by a fan-in-fan-out (FIFO) module and copies were sent to both the analog and the digital DAQ setups, see Fig. 2.4. On the analog side, the signals were processed before time and energy information were sent through an optical link to a computer running Centos 7.3 where it was written to hard drive.

Constant-Fraction Discriminators

The YAP and NE213 pulses were sent to constant-fraction discriminators (CFDs), labeled ① in Fig. 2.4. CFDs were used because ToF measurements require precision timing of the start and stop signals. Simply triggering on the leading edge of pulses will lead to "time walk" for similarly shaped pulses of varying amplitudes. Time walk means that pulses of the same shape but different amplitude will result in triggers at different times, see Fig. 2.6. As can be seen, the smaller pulse passes the threshold at a later time than the larger pulse. By instead triggering on the point where a pulse reaches a certain fraction of its peak amplitude, time walk can nearly be eliminated [3]. This may be achieved by dividing or copying the signal, inverting one copy and delaying the other. The pulses are then added and the zero crossing of the summed signal corresponds to a fraction of the input pulse, see Fig. 2.7. Changing the amplitude of the incoming signal will have the

same effect on both copies of the signal. Consequently the CFD trigger time, defined by the zero-crossing, is amplitude independent. The output of the CFD was a logic pulse representing the trigger time of the CFD. CFDs were also used to enforce an amplitude threshold of 94.6 mV for the NE213 detector and 25.0 mV for the YAP detector. Only pulses above the thresholds generated logic pulses.

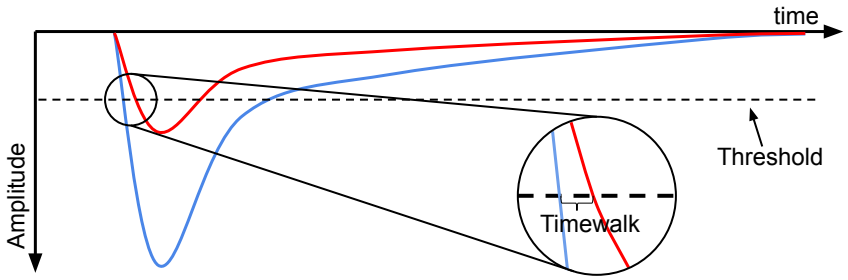

Figure 2.6: Time walk resulting from leading-edge triggering. Figure adapted from Ref. [13].

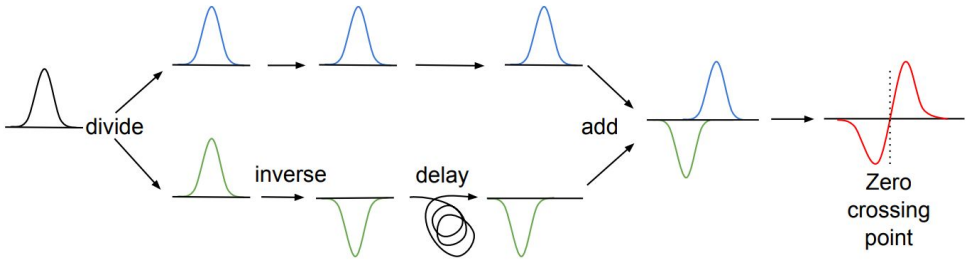

Figure 2.7: CFD trigger principle. Figure from Ref. [13].

Trigger Logic

The NE213 logic pulses generated by the CFD were sent to a latch (labeled ② in Fig. 2.4), which allowed a single pulse to pass at a time and blocked any further pulses until it received a reset signal. The pulses that made it through were passed on to the data-acquisition modules presented below. The reset signal was given after the data-acquisition modules had finished digitization (∼10 µs) and the data has been written to a computer via optical link (∼350 µs). The amount of time the latch was closed is called the deadtime. This is because the system is unable to process new events (effectively dead) during this time. The deadtime was measured by an uninhibited and an inhibited scaler connected to a pulser. A scaler is a module which simply counts the number of logic pulses it receives. The pulser incremented the scalers at a specific frequency. Whenever the latch was closed, the inhibited scaler was no longer incremented. This made it possible to calculate the livetime as the ratio of inhibited scaler counts to uninhibited scaler counts every time the scalers were read. Note that although the setup contained both YAP and NE213 detectors, only the NE213 detector was used to trigger the acquisition.

Since ToF measurements require both a start and stop signal, there can at most be as many coincidences as there are pulses in the detector with the lowest count rate. The NE213 detector experiences the lowest count rate. Thus, the deadtime was minimized by triggering the acquisition on the NE213 detector.

Time-to-Digital Converters

A logic signal was also sent from the latch to a time-to-digital converter (TDC). This module is labeled ③ in Fig. 2.4. The TDC charges a capacitor with a constant current once a start signal is received, and stops once the stop signal is received. The start signal is the event logic pulse from the NE213 detector and the stop signal is a delayed event pulse from the YAP detector. The amplitude of the capacitor-discharge pulse is proportional to the time between the start and stop signals [14]. An analog-to-digital converter within the TDC digitizes the pulse and sends the resulting number to the computer via an optical link.

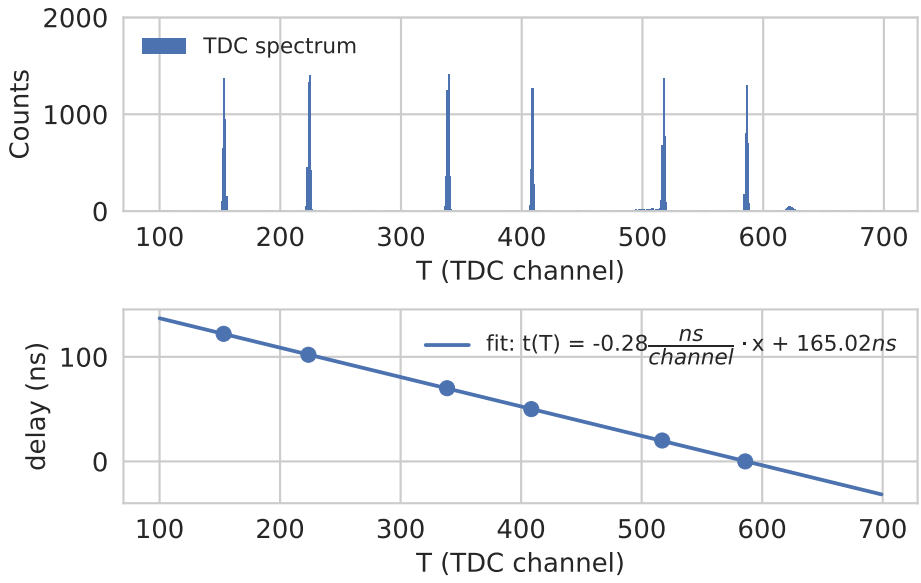

Figure 2.8: TDC calibration spectrum. Top panel: Each peak represents a different delay value for the stop pulse. Bottom: A linear fit applied to the TDC and delay values.

The raw values provided by the TDC had units of TDC channels, so a calibration was necessary to convert them into ns. By triggering the start of the TDC with a delayed version of the same signal used to stop the TDC, a very sharp peak was produced. This peak was then shifted over known intervals by increasing delay-cable length to produce the calibration data shown in Fig. 2.8. Since the location of $t = 0$ is arbitrary, the important result is the calibration coefficient 0.28 ns/channel which was used to convert timing data from TDC channels to ns.

Charge-to-Digital Converters

The pulses that made it through the latch were used to generate 60 ns and 500 ns logic pulses with the first 25 ns preceding the CFD trigger point. These pulses acted as integration "windows" or "gates" for the charge-to-digital converters (QDCs). In Fig. 2.4, these modules are labeled ④. Copies of the analog current pulses were also sent to the QDC modules. Each module carried out an integration for the duration of the applied gate. The resulting charges provided a measure of the energy deposited in the detector by a given pulse on two different timescales. The QDC modules sent their outputs via optical link to a computer where they were written to the hard drive, see Fig. 2.4.

The charge integration performed by the QDC modules is a measure of the energy deposited in a detector. In the NE213 detector, neutrons interact primarily via scattering from ^{1}H while gamma-rays interact primarily with atomic electrons. It is customary to calibrate a fast-neutron detector with gamma-ray sources, employing the "electron-equivalent energy". Electron-equivalent energy corresponds to the amount of energy deposited by an electron. As gamma-rays interact with atomic electrons, they result in electron-equivalent deposited energies. One way of performing this energy calibration is the Knox method of examining the Compton edge corresponding to monoenergetic gamma-rays [15]. The maximum energy transferred by a gamma-ray to a recoil electron is given by:

$$(E_e)_{max} = \frac{2E_\gamma^2}{m_e + 2E_\gamma} \, [\mathrm{MeV}_{ee}], \tag{2.1}$$

where $(E_e)_{max}$ is the maximum energy transfered by a gamma-ray to a recoil electron, E_γ is the energy of the gamma-ray and m_e is the mass of the electron. A Gaussian function may then fitted to the region of the Compton edge. The QDC channel where the Gaussian distribution reaches 89% of its height is associated with $(E_e)_{max}$. The 4.44 MeV Compton edge produced by the de-excitation of ^{12}C was used together with the 2.23 MeV Compton edge produced by the de-excitation of ^{2}H for calibration purposes.

Figure 2.9 shows a QDC calibration spectrum produced with a 500 ns integration window. The narrow peak the furthest to the left in Fig. 2.9 is the pedestal. It is produced when the QDC is made to trigger when there is no current pulse in the detector. The pedestal was produced for calibration purposes by allowing a small fraction of the YAP events to trigger the DAQ. It represents the zero point of the QDC spectrum, so for the energy calibration it is associated with 0 MeV_{ee}. All the values used in the calibration are shown in Table 2.1.

QDC(channel)	67.5	1272.1	2718.9
E(MeV)	0	2.23	4.44
$(E_e)_{max}(\mathrm{MeV}_{ee})$	0	2.00	4.20

Table 2.1: Analog energy-calibration data. QDC channels fitted to known Compton edges. See text for details.

The x-axis at the top of the panel shows the calibrated energy scale. The bump

immediately to the right of the pedestal is produced when the YAP trigger coincides by chance with a random deposition of energy in the NE213 detector. The 2.23 MeV and the 4.44 MeV Compton edges have been highlighted in purple and orange. Using the points listed in Table 2.1, a linear calibration fit was made and plotted, see Fig. 2.9 (bottom panel). With this fit, the QDC spectrum was converted from channels to MeV_{ee}. It can be seen that the uncertainty is greatest for the 2.23 MeV Compton edge.

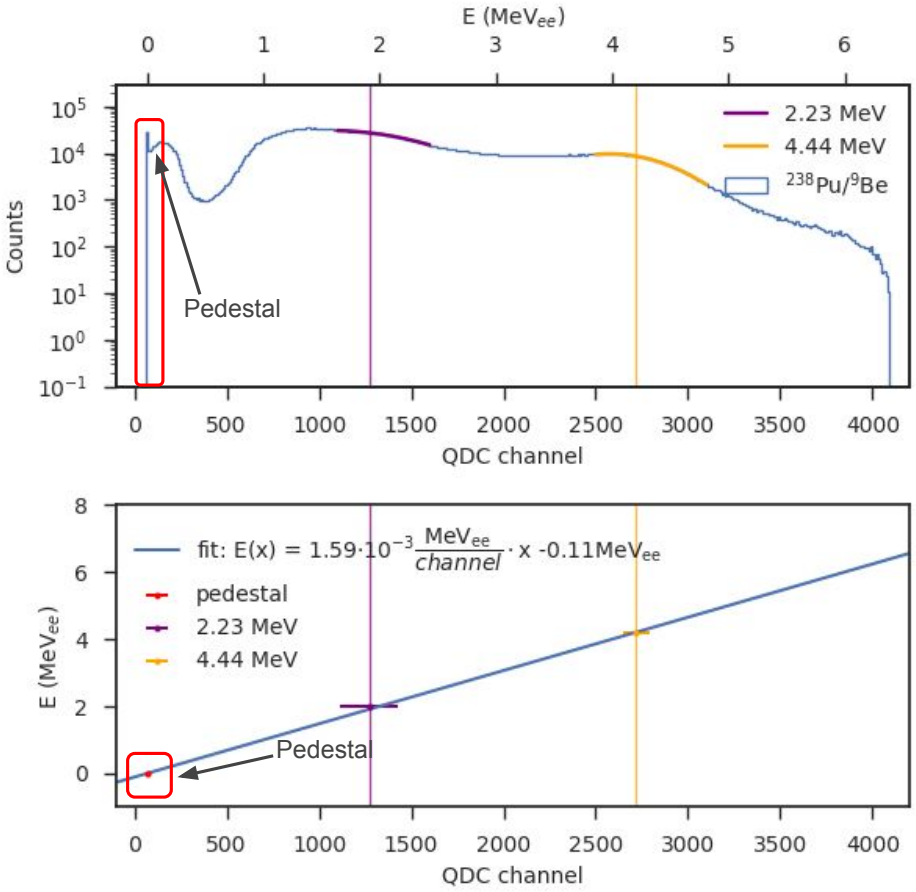

Figure 2.9: QDC calibration of the analog setup. Top panel: Pu/Be spectrum measured using the NE213 detector. The upper x-axis has been calibrated. Bottom panel: The calibration fit produced with the Knox method. The pedestal is indicated with a red box in both plots.

Charge-Comparison Pulse-Shape Discrimination

The CC method was implemented by integrating the pulses in the NE213 detector over a LG window of 500 ns and a SG window of 60 ns. As described in Sec. 1.2.4, the constants a and b were tuned to optimize the separation between the neutron and gamma-ray bands.

2.2.2 Digital

Digitizer Specifications and Configuration

A digitizer is an electronic device which converts analog signals to digital waveforms. A continuous analog signal is approximated by a list of numbers, each representing a single sampling point, along with additional information such as a time stamp based on a global clock and the channel number of the signal. An acquisition is triggered when the amplitude of the input signal crosses a configurable threshold value. By this definition, a digitizer is similar to a digital oscilloscope. The main difference is that the oscilloscope has a display and is optimized for portability and realtime diagnostic use, whereas the digitizer is optimized for efficient high-rate data transmission to a computer where further analysis can be carried out, either online or more commonly offline. The advantage of a digitizer over a traditional analog DAQ system is that it allows the user to process a single data set in multiple ways in order to optimize the parameters of the acquisition, without having to change anything in the physical setup or acquire subsequent data. The disadvantage is that the quality of the discretization of a continuous signal is limited by the sampling rate, dynamic range, resolution and bandwidth of the digitizer as well as the data-transfer rate of the read-out system. The sampling rate is the frequency at which the digitizer samples a signal. The higher the sampling rate the better the digital representation of the original analog signal, see Fig. 2.10. The dynamic range is the difference between the minimum and maximum voltage the digitizer can record. The resolution defines the number of partitions the dynamic range is divided into and is typically given in bits. The bandwidth determines which signals a digitizer can reproduce without significant alteration. Signals whose Fourier expansion contain higher-frequency components will require greater bandwidth[2]. The data-transfer rate defines how fast the digitizer can transfer data to a computer. Low data-transfer rate will lead to greater deadtime.

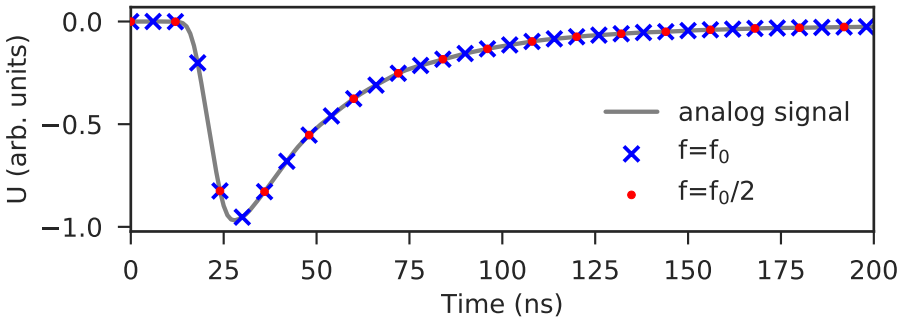

Figure 2.10: Sampling rate. Illustration of an analog signal sampled with two different sampling rates, f_0 and $f_0/2$.

[2]For example, the perfect digitization of a square wave will require an infinite bandwidth, as its Fourier expansion is an infinite sum.

The digitizer used in this work is an 8 channel CAEN VX1751 waveform digitizer. It has a sampling rate of 1GS/s in standard mode, but can also be operated in double-edge sampling mode, which disables 4 cannels but increases the sampling rate to 2 GS/s [16]. The data presented in this thesis were acquired in standard mode. This resulted in one data point per ns when digitizing signals. Given a set of sample points, there will always be an infinite number of waveforms that fit the points [17]. This is called aliasing. Nyquist's theorem states that if the sampling rate is at least twice as large as the highest frequency component of the signal, aliasing may be avoided [17]. An even higher sampling rate is typically desirable. If the sampling rate is too low, important features such as peak location and amplitude will be less well defined, see Fig 2.10. In order to reproduce signals accurately, it is not enough to have a high sampling rate. The dynamic range, resolution and bandwidth also need to be considered. The VX1751 digitizer has a 1 V dynamic range, which means that the difference between maximum and minimum voltage is 1 V. This is controlled through the choice of signal polarity and baseline offset. The resolution of the digitizer is 10 bits, so the 1 V dynamic range is divided into 1024 bins each of size 0.978 mV [16]. The VX1751 has a bandwidth of 500 MHz [16]. The bandwidth is important because it determines the frequency range of signals that can be digitized without significant attenuation. If the frequency components as obtained from a Fourier expansion of the signal are too high, then the amplitude recorded by the digitizer will be lower than the actual amplitude of the input signal. A rule of thumb for evaluating the bandwidth needed by a given signal is:

$$B = 0.35/T_{\text{rise}}, \tag{2.2}$$

where T_{rise} is the time it takes the pulse to rise from 10% to 90% of peak amplitude and B is the bandwidth for which the signal is attenuated to only 70% of the original amplitude [3]. Thus, with a 500 MHz bandwidth, the VX1751 will cause 70% attenuation in signals with 0.7 ns rise time. Since the signals studied here have rise times on the order of 5−15 ns, bandwidth is not a limitation.

The digitizer was connected to a computer running Centos 7.4 via an optical link. This connection supports transfer rates of 80 MB/s [16]. However the number of events transfered at a time is also a limiting factor. In this work, the data were transferred on an event-by-event basis, which led to a significant reduction in livetime, see Chap. 3. The digitizer is controlled by WaveDump version 3.8.1 published by CAEN under the terms of the GNU General Public License [18]. It uses the proprietary digitizer control libraries, also published by CAEN[3]. WaveDump configures the digitizer according to a text file supplied by the user. The number of data points per trigger is defined globally for all enabled channels. The signal polarity, trigger threshold and baseline offset also need to be defined. The trigger threshold is the minimum amplitude relative to the baseline that a pulse must have to be recorded. The baseline offset determines where in the dynamic range of the digitizer the baseline is placed. A baseline offset of 0% will

[3]The version used in this work was modified to write all data to a single file rather than one file per channel.

cause the entire range to be used for pulses of the selected polarity. This means that undershoot will not be seen. Therefore it is best to use a small baseline offset. The NE213 detector was connected to channel 0 of the digitizer and the YAP detector was connected to channel 1. Both the resulting NE213 and YAP pulses were of negative polarity. An amplitude threshold of 48.8 mV was applied to the NE213 detector signals and a threshold of 9.8 mV was applied to the YAP detector signals. A baseline offset of 40% was inadvertently applied to the NE213 channel and a baseline offset of 10% was applied to the YAP channel. This meant that high amplitude NE213 pulses were clipped while high amplitude YAP pulses were not. The pulses thus saturated the dynamic range of the digitizer resulting in a small subset of large pulses with a flat top.

For a one hour run with the NE213 detector placed 1.05 m from the Pu/Be source and one YAP detector connected, data corresponded to ∼120 GB text file. The Python library Dask was used for processing the data because it is optimized for processing datasets that are too large to fit in random-access memory. It also runs on all available processor cores [19]. After processing and data reduction, the data were saved to a binary file of size 7.3 GB . The Python library Pandas was used for additional processing and the visualization of the reduced data set [20][4].

Time Stamping

The digital setup needs a method for providing a time stamp for each pulse from the detectors. A global time stamp is provided by the digitizer for each acquired waveform or "event". However, each event is 1204 ns long, and the pulses do not begin at the exact same point in time within the acquisition window. This is because the trigger clock triggers on the leading edge of pulses and runs at only 125 MHz, whereas the sampling rate is 1 GHz. Consequently, it was necessary to precisely determine where in the sampling window the pulse was located. For this purpose, a software-based CFD algorithm was implemented. The algorithm searched the first 40 ns before the maximum amplitude of the pulse for the first sampling point to rise to 30% of the maximum amplitude. Linear interpolation between this sampling point and the previous sampling point enabled a time stamp with resolution better than 1 ns to be generated. In Fig. 2.11, four pulses from the NE213 detector are plotted centered around their CFD trigger points. Although this time stamp is given with sub-ns precision, the accuracy is limited by the determination of the pulse amplitude, which in turn is limited by the sampling rate, resolution and bandwidth.

Data Selection

As the digitizer only enforced a threshold, additional selection criteria were applied offline to filter the data set. Since the VX1751 triggered on all enabled channels simultaneously, all empty acquisition windows were discarded. This was done by determining and subtracting a baseline for each waveform. The baseline was determined by averaging over

[4]Python version 3.6.3 was used with Pandas version 0.23.4 and Dask version 1.0.0.

the first 20 ns of the waveform. The peak amplitude relative to this new baseline was then determined. An amplitude threshold of 24.4 mV was enforced removing all pulses of amplitude below this value (negative polarity pulses).

During the digitizer configuration, a baseline offset that was too high was inadvertently applied. This meant that only 60% of the dynamic range was available for signals from the NE213 detector. Events whose amplitude could not be contained in the available range had their peaks clipped. These 5.7% of the data were not discarded, but affected the QDC spectrum. The pulse-height spectrum shown in Fig. 2.12 highlights the clipped events in green.

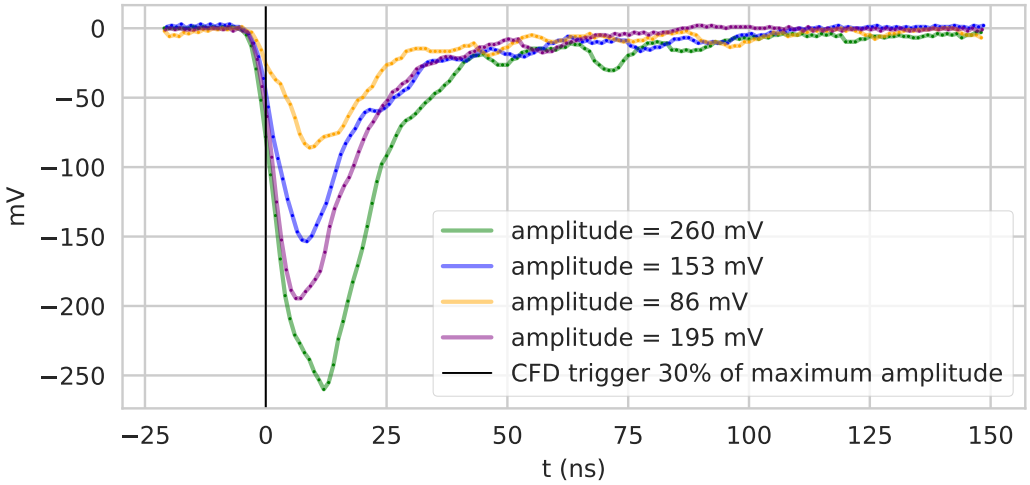

Figure 2.11: Relative timing for NE213 detector pulses of different amplitudes. A CFD algorithm was used to generate a precise time stamp. A CFD trigger level of 30% of the maximum amplitude was used.

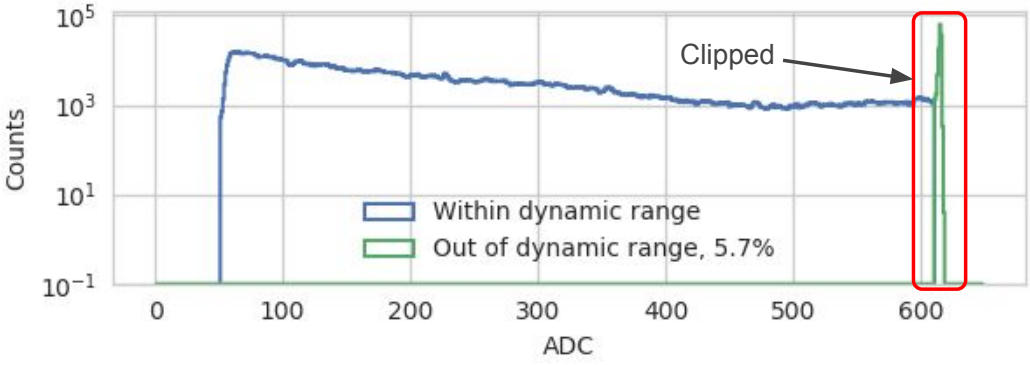

Figure 2.12: Digitized pulse-height spectrum from the NE213 detector. Clipped events which reached the limit of the dynamic range are highlighted in green.

Description	Percentage of events	Discarded
Pulses were clipped	5.7%	No
Unstable baseline	2.7%	Yes
CFD trigger in baseline determination window	$\ll$0.1%	Yes
CFD trigger too late for long-gate integration	1.1%	Yes
CFD algorithm failed	$\ll$0.1%	Yes

Table 2.2: Summary of problematic events. In general the dataset was very healthy.

Certain events were removed because they caused either the baseline determination, pulse integration or CFD algorithm to produce spurious results. For example, in the case of 2.7% of all events above trigger threshold, the baseline determination was deemed unsteady, see Fig. 2.13 (a). Events were removed when the standard deviation of samples in the baseline-determination window was greater than 2 mV. A subset of the times this happened was because a pulse was located inside the baseline-determination window as shown in Fig. 2.13 (b). This was identified when the CFD trigger point was located within the first 20 ns and happened 0.0016% of the time. Figure 2.13 (c) shows a situation where the CFD triggered so late in the acquisition window that not enough samples followed to carry out the 500 ns LG integration. This occurred in 1.1% of the events. And finally, 0.00066% of the events were filtered because a peak was immediately preceded by a smaller peak, see Fig. 2.13 (d). Since the CFD algorithm searched the 40 ns immediately prior to the peak amplitude, it may have triggered due to the preceeding smaller pulse. All of the identified types of problematic events are summarized in Table 2.2.

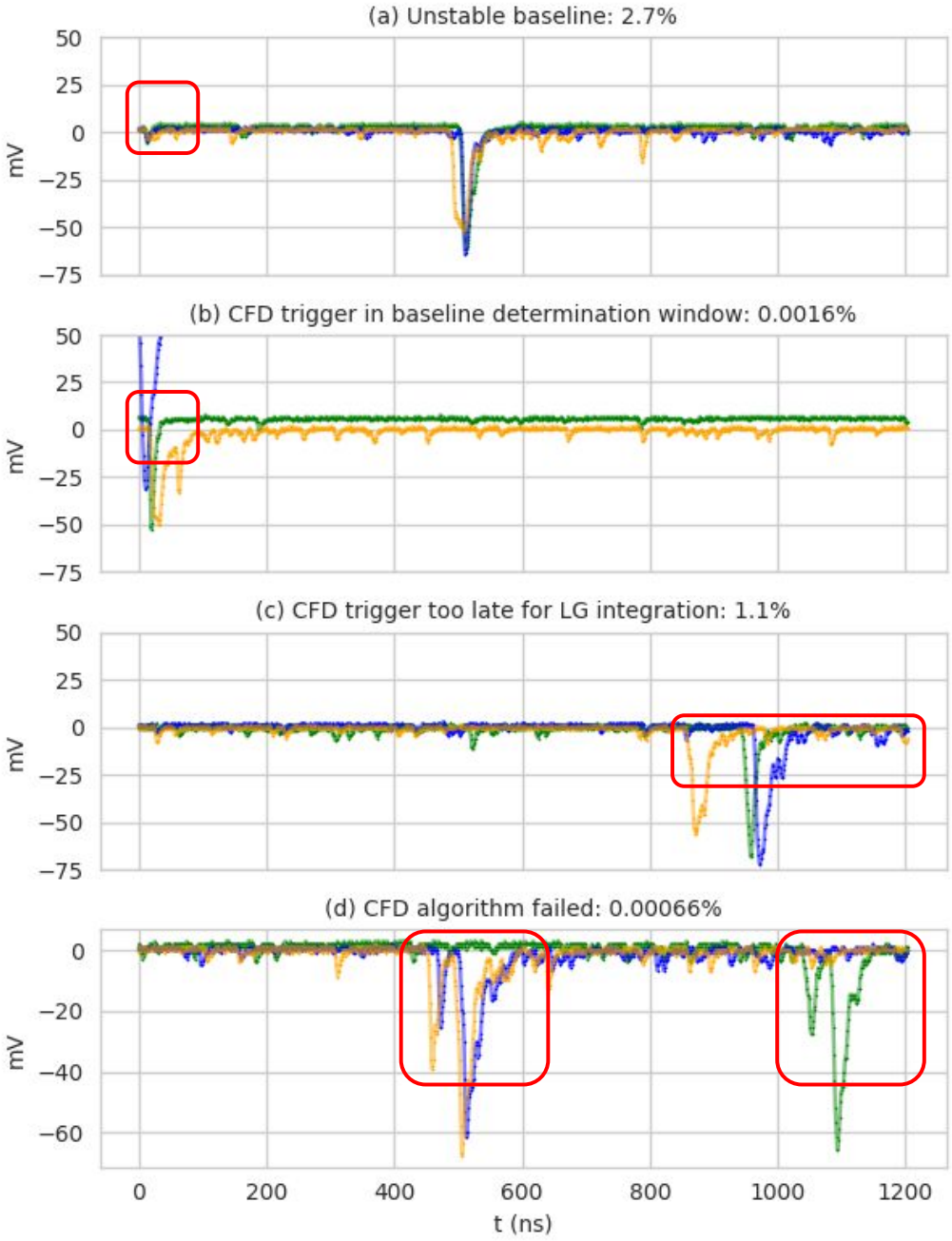

Figure 2.13: Examples of rejected digitized events. Regions-of-interest are highlighted with red boxes. (a) The baseline was deemed unstable. (b) A pulse was located inside the baseline-determination window (a subset of (a)). (c) Less than 500 ns follow the CFD trigger point, so the LG integration could not be carried out. (d) Closely adjacent pulses caused the CFD algorithm to fail.

Energy Calibration

The energy calibration of the digital setup was carried out in a manner similar to the analog setup, using the Knox method. The pulses were integrated digitally over the exact same gate lengths used in the analog setup, namely 60 and 500 ns starting 25 ns before the CFD trigger. A major difference compared to the analog setup was in the baseline determination. For the analog setup, the pedestal was needed by the energy calibration to account for and subtract any baseline offset. It acted as a global baseline subtraction. This was not necessary in the digital setup since the baseline was subtracted on an event-by-event basis during the initial data processing.

Both the Compton edges corresponding to 2.23 MeV and 4.44 MeV gamma-rays produced by the Pu/Be source as well as a Compton edge corresponding to 1.33 MeV gamma-rays from a ^{60}Co source were used for the calibration. The calibration points are listed in Table 2.3. In Fig. 2.14, the Compton edges corresponding to 1.33 MeV, 2.23 MeV and 4.44 MeV gamma rays are marked in red, purple and orange respectively. The ^{60}Co source produces gamma-rays of 1.17 MeV and 1.33 MeV, but due to energy resolution only the Compton edge corresponding to 1.33 MeV is visible. As with the analog setup the uncertainty is the greatest for the 2.23 MeV Compton edge. The baseline shift on the

channel (mV·ns)	3791.4	7079.6	15480.9
E_γ (MeV)	1.33	2.23	4.44
$(E_e)_{max}$ (MeV$_{ee}$)	0.96	2.00	4.20

Table 2.3: Digital energy-calibration data. Digitizer pulse integration channels fitted to known Compton edges. See text for details.

NE213 channel offset was set too high, restricting the range available to negative pulses to only 0.6 V. This affected the Compton edge of the 4.44 MeV gamma-ray. In spite of this problem, Fig. 2.14 shows that the calibration points still follow a linear trend within uncertainty. The fit parameters were used to produce the calibrated x-axis in the upper panel.

Charge-Comparison Pulse-Shape Discrimination

The CC method was implemented in the digital setup by integrating the waveforms over 60 ns and 500 ns gates respectively, starting 25 ns before the CFD trigger. The exact same gate lengths and timing employed by the analog setup were used here to facilitate a direct comparison of the two setups. In addition, the separation between neutron and gamma-ray distributions was linearized by fine tuning the parameters a and b as shown in Fig 1.3.

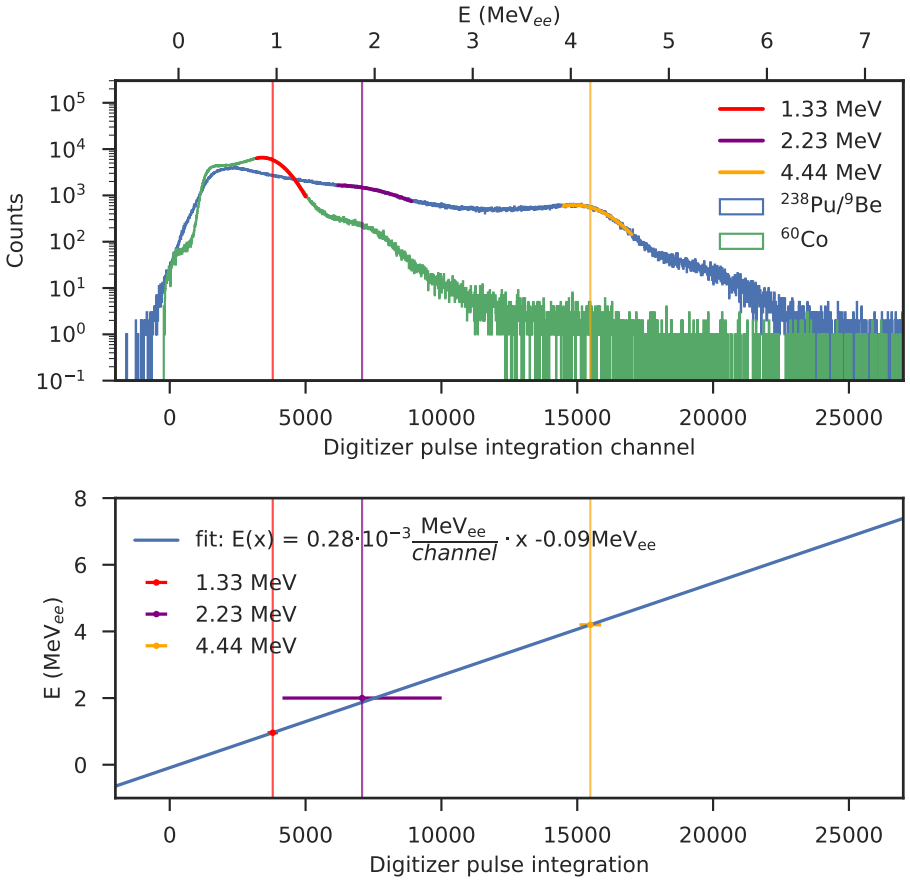

Figure 2.14: Energy calibration of the digital setup. The Compton edges corresponding to the 1.33 MeV gamma-ray from ^{60}Co and the 2.23 MeV and 4.44 MeV gamma-rays from the Pu/Be source have been used to perform the energy calibration.

2.3 Convolutional Neural Network

The biggest advantage a digitizer offers is that it records the entire pulse rather than just extracting a few parameters from it. With the entire waveform available, PSD can be approached in ways that are not feasible with analog electronics. One such approach is to apply an artificial neural network to the task of discriminating between neutrons and gamma-rays. Artificial neural networks are function approximators which use learned parameters called weights to perform a specified task. There are a variety of different network types. For image classification tasks such as PSD, convolutional neural networks (CNNs) set the gold standard. Training neural networks to perform neutron/gamma-ray PSD is not a new approach. It has been successfully implemented in a number of studies for various scintillators, see Ref. [21]. The key difference between what has previously been done and what is done within this thesis lies in the manner the training data were selected.

2.3.1 Training Dataset

To train a network to discriminate between neutrons and gamma-rays, a set of digitized waveforms along with labels defining the species of each waveform is needed. One approach would be to create a precise simulation and train the network on the simulated data. Then the labels are known with certainty to represent the waveforms to which they are assigned. On the other hand, the simulated data must be an excellent representation of actual detector signals. This also implies that new simulations will be needed for new detectors. Another approach is to use different PSD techniques for labeling data as either neutrons or gamma-rays. This is the approach taken by Griffiths et al. [21]. They label their training data by plotting the number of samples within a given pulse that surpasses a certain threshold as a function of peak amplitude, and then making a cut to separate neutrons from gamma-rays. This approach is effective as long as the model used to generate the training data is not systematically mislabeling a certain type of pulses, such as pulses in a certain energy range.

The approach taken here has been to take advantage of the extra information given by the ToF spectrum. The ToF spectrum provides access to a labeled set of neutron and gamma-ray pulses in the form of the neutron bump and the gamma-flash, see Fig 2.15. The downside of this approach is that the ToF spectrum will also contain random coincidences, which means that the training data will contain some neutrons mistakenly labeled as gamma-rays and vice versa. Since the background is composed of random coincidences and makes up only a small amount of the total training data, it is anticipated that the false neutrons/gamma-rays will not cause the network to systematically misclassify, but merely slow down the training.

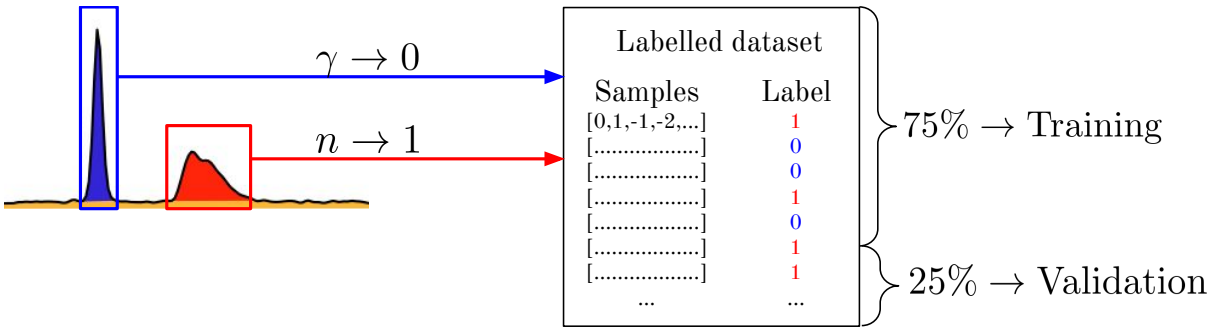

Figure 2.15: Selection of training and validation data using ToF information. Gamma-flash events are labeled 0 and events from the neutron bump are labeled 1.

2.3.2 How It Works

CNNs use kernels of weights to extract features from an input image. The essential features of a kernel are the size, the stride and the weights. Figure 2.16 shows an example of a kernel being applied to an input vector $\vec{x}$. When applying the network to PSD, $\vec{x}$ will be a digitized current pulse from the NE213 detector. In Fig. 2.16, the convolution is

performed with stride 2, i.e. the kernel is moved across the input in steps of 2. The kernel takes a single input vector and operates on 3 elements at a time, so it has dimensions 1×3. The elements ω_i of the kernel are called weights. The kernel is scanned across $\vec{x}$ and a new vector or feature map $\vec{h}$ is produced. Each element of $\vec{h}$ is provided by a function ϕ which takes the scalar product of the kernel and a segment of $\vec{x}$ along with a bias b as input, see Fig. 2.16. $\vec{\omega}$ and b are the parameters which will be optimized through training. A common choice of activation function for CNNs is the rectified linear unit, ReLU given by:

$$\mathrm{ReLU}(x) = \begin{cases} 0, & \text{if } x < 0 \\ x, & \text{otherwise.} \end{cases} \tag{2.3}$$

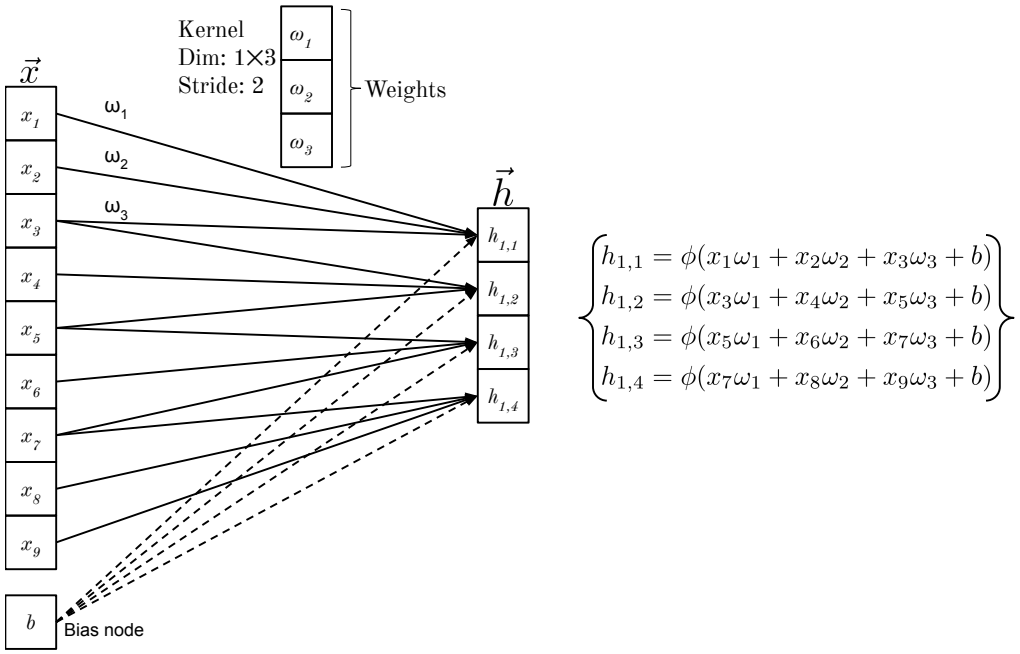

Figure 2.16: Convolution of a vector and a kernel. Connections from the bias node are marked with a dashed line.

Convolutional neural networks typically employ multiple layers each containing multiple filters, see Fig. 2.17. Note that Fig 2.17 is drawn to illustrate how a CNN works and does not reflect the exact architecture of the network employed in this thesis. The first operations carried out in this network is marked with ① and are convolutions. Three kernels are applied to the input vector to produce three new feature maps in exactly the same manner as was shown in Fig. 2.16. The job of each filter is to highlight simple features in the input vector.

The next operations labeled ② are also convolutions. This time four kernels are scanned across the red, green and blue feature maps from the preceeding layer. Each of the four filters have dimension 3×2, meaning that they operate on two elements in each feature map simultaneously, in order to extract more complex information. This produces

the four new feature maps $\vec{g}_1$, $\vec{g}_2$, $\vec{g}_3$, $\vec{g}_4$. The next operation labeled ③ is a flattening of the four feature maps into a single vector $\vec{f}$. In the final operation labeled ④, the output y of the network is given by an activation function ϕ_{out}, which takes a linear combination of the elements of $\vec{f}$ as input. For binary classification problems, a common choice of activation function ϕ_{out} is the logistic function, which is bounded between 0 and 1:

$$\phi_{out}(x) = \frac{1}{1+e^{-x}}. \tag{2.4}$$

This function allows the output to be interpreted as a probability of the input waveform $\vec{x}$ representing a neutron.

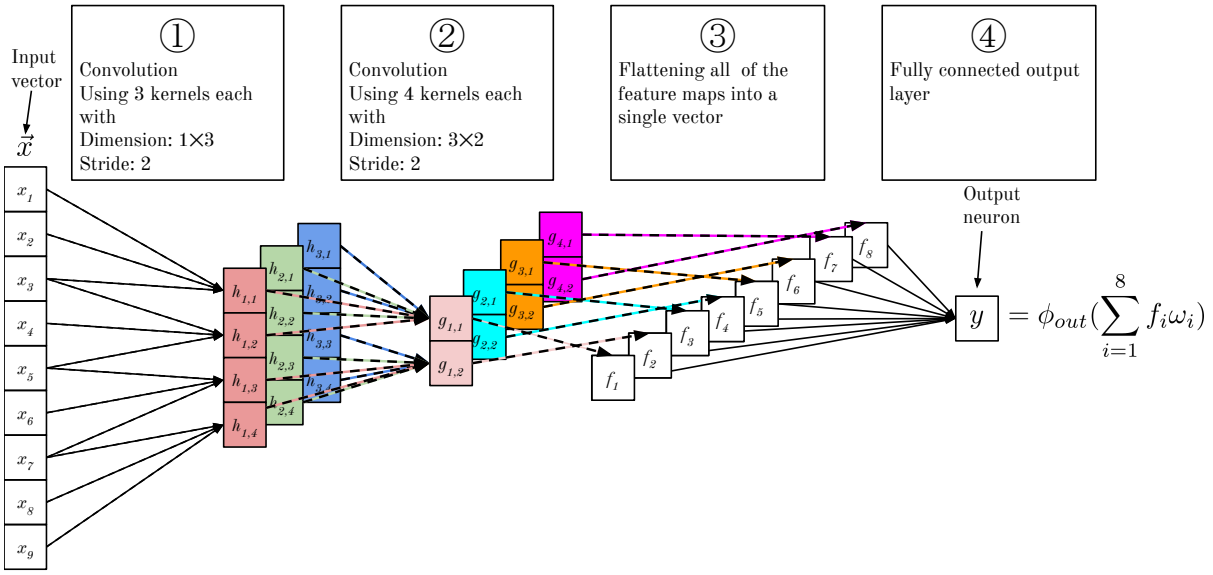

Figure 2.17: Two-layer CNN. Each of the feature maps in the convolutional layers are produced with a unique kernel, and has been given its own color. For readability, only connections to the red and pink feature maps are shown. The other feature maps are connected in the same manner. Bias nodes have also been omitted for readability.

The output of the network will be useless unless the weights have been properly trained to extract relevant features. The network is trained through a simple yet incredibly powerful method called "backpropagation". In backpropagation, the derivative of an error function with respect to each weight in the network is found through repeated use of the chain rule. These derivatives are then used to make adjustments to the weights in order to minimize the error function. The error function used in this work is the binary cross-entropy error function. It is commonly applied to binary classification tasks and is given by:

$$E = -\frac{1}{N}\sum_{n}^{N} \left(d_n \log(y(\vec{x}_n)) + (1-d_n)\log(1-y(\vec{x}_n))\right). \tag{2.5}$$

This function calculates the average error E over N input vectors $\vec{x}_n$ with labels d_n. y_n

is the output of the network. In the case of neutron/gamma-ray discrimination, each vector $\vec{x}_n$ will be a digitized waveform. If $\vec{x}_n$ represents a neutron, then $d_n = 1$ and the second term disappears. If instead $\vec{x}_n$ represents a gamma-ray, then $d_n = 0$ and the first term disappears. After propagating N waveforms through the network, the weights can be updated using the derivatives of the error function. A simple updating method is the stochastic gradient descent updating rule:

$$\omega_i^{t+1} = \omega_i^t - \eta \frac{\partial E^t}{\partial \omega_i}, \tag{2.6}$$

where ω_i is weight i in the network, E is the error function and t is the training iteration. The constant η is a scaling factor called the "learning rate". It scales the corrections down to avoid overshooting optimal weights. The procedure is repeated until the error function has converged at a minimum value.

2.3.3 Implementation of the Network

A CNN was implemented using KERAS version 2.2.4[5] [22]. The main features of the chosen architecture are summarized in Table 2.4. In addition to convolutional layers, this network also contains "max pooling" layers. Max pooling layers reduce the size of each feature map individually by passing on only the maximum value of a given neighbourhood of the input vector. With a size of 2 and stride of 2, input vectors are reduced to half their size, see Fig. 2.18. Due to the kernel size and stride as well as the max pooling, each node in the flattened layer is indirectly connected to a large number of samples in the input layer. Both convolutional layers employ the ReLU activation function, while the final layer applies the logistic function.

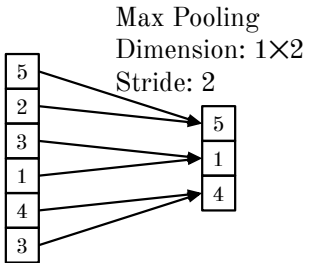

Figure 2.18: The Max pooling principle.

The network was trained on events from the gamma-ray and neutron ToF peaks of a 75 minute data set. This data-set was not used for any further analysis. 300 samples (or equivalently ns) from each pulse were used starting 20 ns prior to the CFD trigger point. 75% of the pulses or 3018 events from the neutron bump and 3018 events from the gamma-flash were used as labeled training data while the remaining 25% were used to

[5]KERAS is a high-level framework for constructing deep-learning models in PYTHON. It can be run using different backends for carrying out operations on tensors. Here TENSORFLOW 1.12.0 was used as a backend.

Input layer: dimension 1×300				
Hidden layers	Kernel Dimension	N kernels	Stride	Activation function
Convolutional layer	9×1	10	4	ReLU
Max pooling	2×1	-	2	-
Convolutional layer	5×10	16	2	ReLU
Max pooling	2×1	-	2	-
Fully connected: dimension 1× 144				
Output layer: dimension 1×1, activation function: $\phi_{out}(x) = \frac{1}{1+e^{-x}}$.				

Table 2.4: Parameters essential to the CNN.

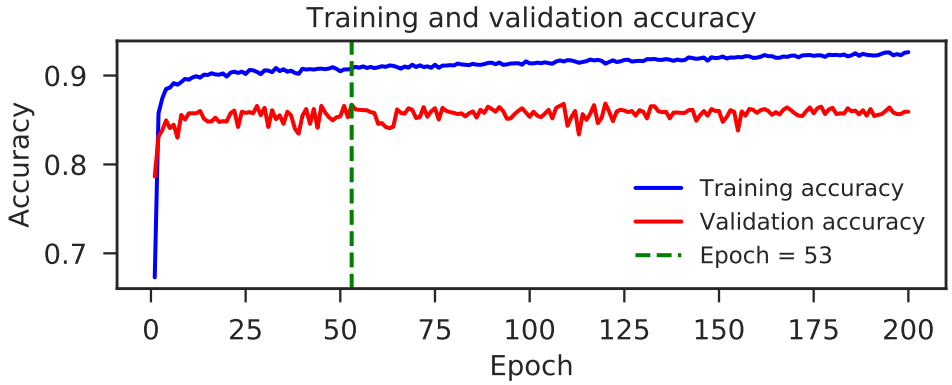

Figure 2.19: Training and validation accuracy of the CNN. The dashed line indicates the epoch corresponding to the chosen model.

evaluate the model, see Fig. 2.19. Here the accuracy of the model, defined as the fraction of correctly labeled events, is plotted as a function of the epoch, with epoch defined as the number of times the network has trained on the entire training dataset. The blue curve shows the fraction of correctly labeled pulses achieved on the training data as a function of iteration, while the red curve shows the same thing on the validation data. The red curve varies more since it represents a smaller dataset. As both training and validation data contain some fraction of incorrectly labeled background events, the model is not expected to reach 100% accuracy on either data set. This plot shows that although the performance on the training set keeps increasing, the performance on the validation set quickly levels out. For this reason, the model achieved at iteration 53 is used. The network is still learning beyond iteration 53, but it is no longer learning features that generalize to the validation data. It is instead overfitting to noise in the training data.

2.3.4 Decision Study

One way to gain a deeper understanding of how the CNN distinguishes between neutrons and gamma-rays is to examine the pulses classified with a high level of confidence. Figure

2.20 shows examples of pulses classified with more than 95% confidence. The pulses labeled as neutrons decay more slowly than those labeled as gamma-rays. This is in agreement with expectations as fast neutrons give rise to recoiling protons in the NE213. These recoiling protons tend to activate slow scintillation-light components more than electrons do.

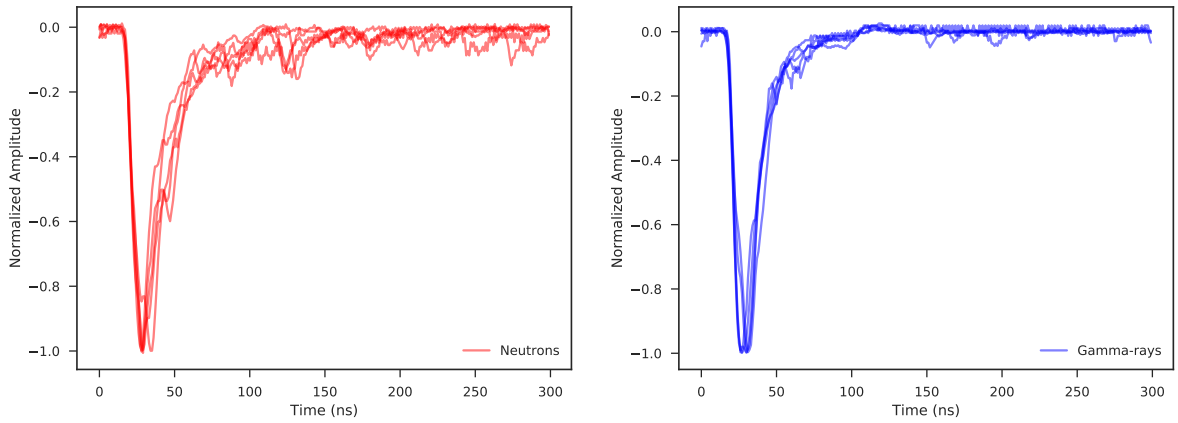

(a) Neutron pulses.

(b) Gamma-ray pulses.

Figure 2.20: Pulses classified by the CNN with more than 95% confidence.

Examining pulses the network had trouble with can further explain the decision making process. The CNN was designed to assign a number between 0 and 1 to pulses, with values close to 0 meaning the network is certain it is looking at a gamma-ray and values close to 1 meaning that it is certain that it is looking at a neutron. Figure 2.21 shows a pulse with a prediction value of 0.49, meaning that the network has difficulty determining particle species. By forcing a subset of samples in this waveform to zero, the decision of the network is constrained to the remaining information. The yellow curve in Fig. 2.21 shows the network prediction when a 31 pixel window of zeros or "blanks" is scanned across the pulse. A prediction at a time t in Fig. 2.21 represents the prediction of the network when the 31 samples in the pulse centered around t are set to zero. When blanking the body of the pulse, the prediction rises to around 1, which means the network is convinced it is looking at a neutron, based upon the remaining information in the tail. When the first part of the tail is blanked, the network becomes convinced that it is looking at a gamma-ray, based upon the remaining information. The network has learned that neutrons have a significant fraction of the total charge in the tail of the pulse and that gamma-rays have most of the charge in the body of the pulse.

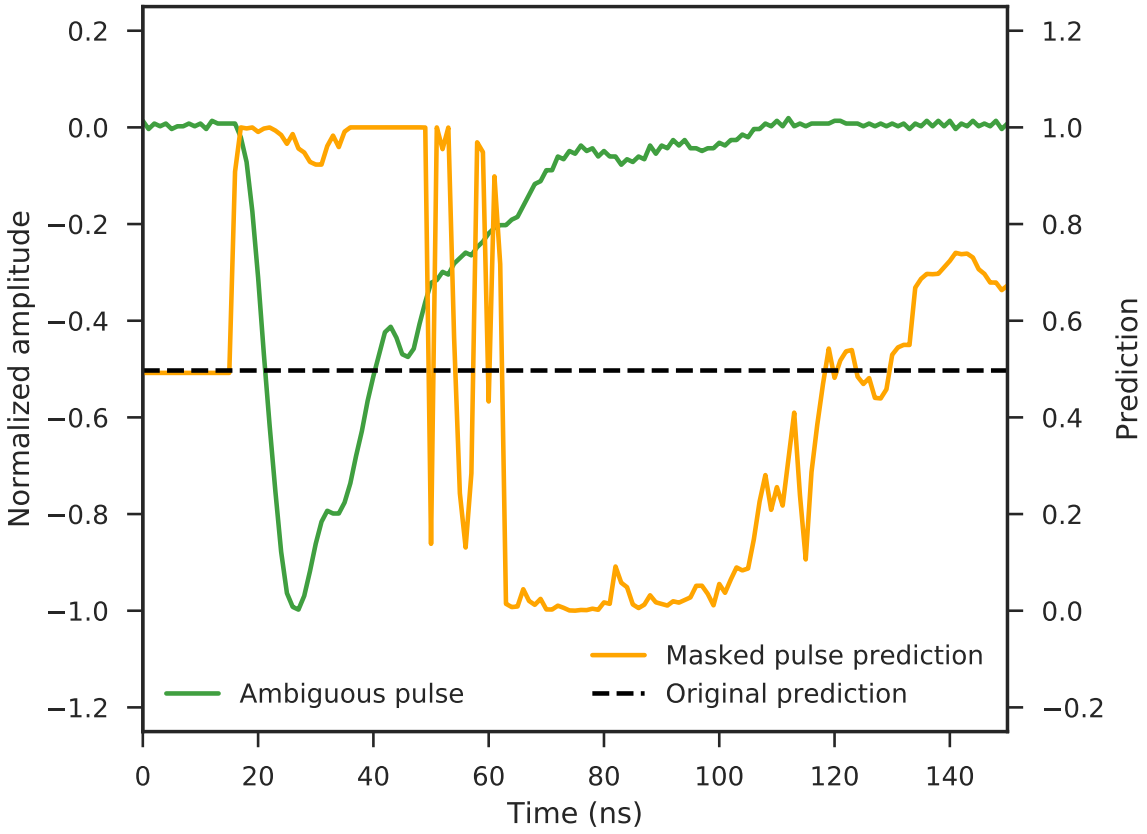

Figure 2.21: CNN decision study. The green curve (left y-axis) shows a pulse the network could not clearly classify as either neutron or gamma-ray. The yellow curve (right y-axis) shows how the CNN prediction varies when part of the pulse is blanked.

Chapter 3

Results

3.1 Data Sets

3.1.1 Overview and Comparison

The data presented here were collected during a one-hour measurement with both the analog and the digital setup running in parallel. A total of 4.3 million pulses from the NE213 detector were recorded by the analog setup. The digitizer saw 2.2 million pulses from the NE213 detector over the same period of time. This large difference in counts was because the digital setup was configured to transfer each event individually, resulting in a very low livetime. In the analog setup, amplitude thresholds of 25.0 mV and 94.6 mV were applied to the YAP detector and the NE213 detector, respectively. In the digital setup, thresholds of 9.8 mV and 48.8 mV were applied to the YAP detector and the NE213 detector, respectively. Having such a low threshold on the YAP detector was found to decrease the signal-to-noise ratio in the ToF spectrum, so a higher threshold of 24.4 mV was applied offline in software. Table 3.1 presents an overview of the data sets.

Setup	YAP threshold (mV)	NE213 threshold (mV)	NE213 events (10^6)	Livetime %
Analog	25.0	94.6	4.3	44
Digital	9.8/24.4*	48.8	2.2	**

Table 3.1: Overview of the analog and digital data sets. *An amplitude threshold of 24.4 mV was enforced offline (see text for details). **The digital setup did not have a method for determining livetime.

3.1.2 Livetime and Threshold Alignment

Deposited Energy

The analog and the digital setups were run with different amplitude thresholds. To properly compare them, a common threshold was necessary. Further, the analog and

digital setups had significantly different cable lengths between the detectors and the electronics. Thus, the signals were attenuated differently before being processed by the different systems. As a result, the required digital-setup threshold was significantly higher than the analog threshold.

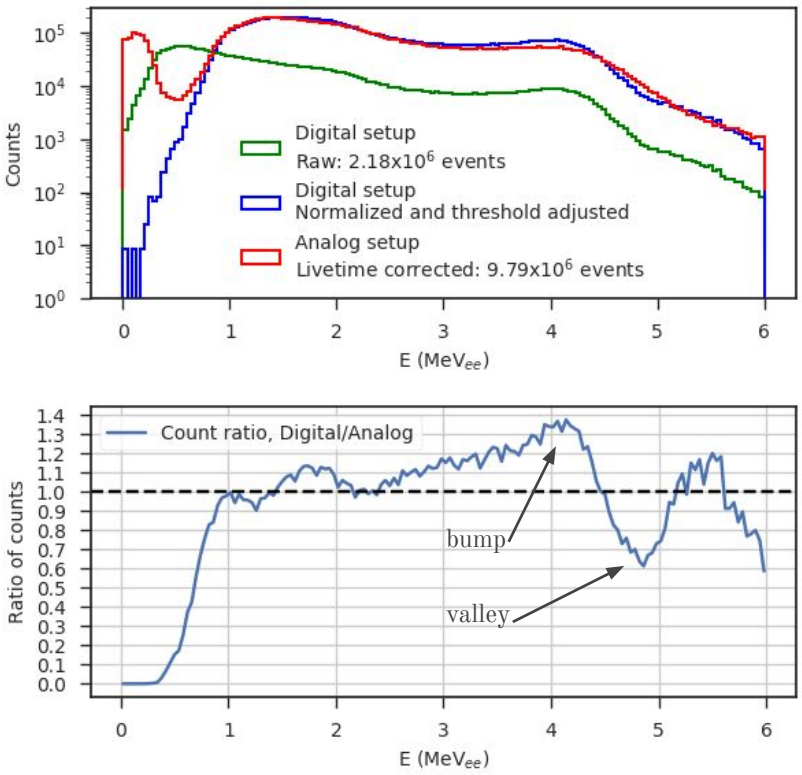

Figure 3.1: Comparison of analog and digital spectra from the NE213 detector. Top: Livetime-corrected analog energy spectrum (red). Raw digital energy spectrum (blue). Digital energy spectrum after threshold matching and normalization (green). Bottom: Ratio of counts between the livetime-corrected analog spectrum and the normalized digital spectrum.

Figure 3.1 (top panel) shows the energy spectra from both setups. The data from the analog setup have been livetime corrected (44%). The blue histogram shows the raw digital spectrum, and the green histogram shows the digital spectrum after applying a higher amplitude threshold of 151 mV in software and normalizing the spectrum to match the height of the livetime-corrected analog setup. The resulting red and green spectra are far more similar, although the Compton edges associated with the 4.44 $\mathrm{MeV_{ee}}$ gamma-ray do not look exactly the same. This may be because some of these gamma-rays deposited energies which exceeded the dynamic range of the digitizer. The livetime of the digital setup can be estimated by scaling the livetime of the analog setup to the ratio of counts in the digital and analog setups. A crude estimate of the livetime of the digital setups is thus 22%. Figure 3.1 (bottom panel) shows the ratio between the digital and analog spectra as

a function of deposited energy after both threshold alignment and normalization. Ideally, this ratio should be unity. This is not the case. Near the Compton edge corresponding to the 4.44 $\mathrm{MeV_{ee}}$ gamma-ray there is a bump and a valley. Again, this may be due to the highest amplitude digitized pulses corresponding to the highest energy Compton scattering events being clipped, causing them to register lower values of deposited energy.

Time-of-Flight Spectra

The ToF spectrum is heavily influenced by the choice of amplitude threshold. Figure 3.2 (top panel) shows ToF spectra for the two setups with the initial 49 mV NE213 detector threshold on data from the digital setup and a 94.6 mV threshold on the data from the analog setup. Interestingly, it seems that the analog setup misses the less energetic neutrons due to the high amplitude threshold. By applying the offline NE213 detector amplitude threshold of 151 mV and the YAP detector threshold of 44 mV to the data from the digital setup and normalizing the data as before, the ToF spectra shown in the bottom panel of Fig. 3.2 are obtained. The neutron peaks now have roughly the same shape, which means that the amplitude cut has also removed these lower energy neutrons.

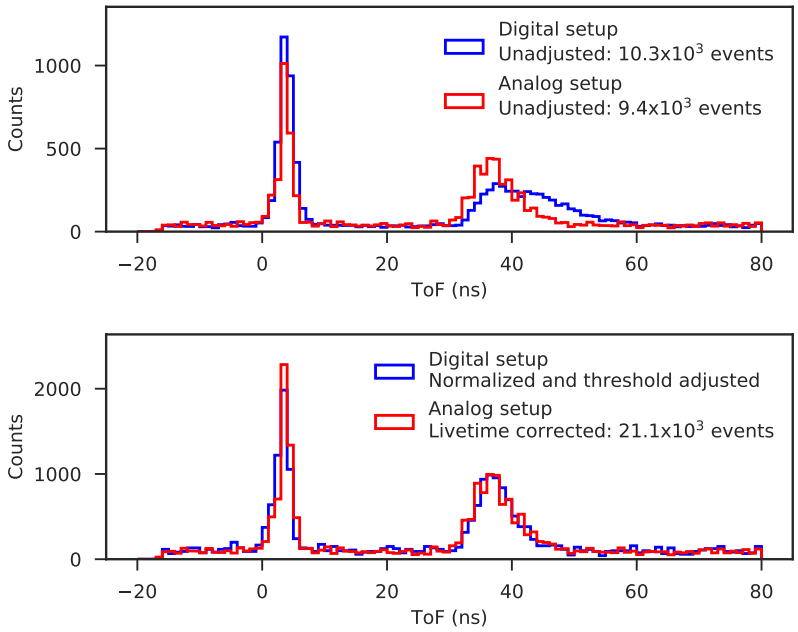

Figure 3.2: Analog and digital ToF spectra. Top: Unadjusted. Bottom: livetime has been taken into account and a higher threshold has been enforced on the NE213 and YAP signals for the digital setup.

3.2 Analog Setup

3.2.1 Neutron Tagging

Figure 3.3 shows the ToF spectrum recorded by the analog setup. The neutron and gamma-ray peaks are indicated. In addition to these two peaks, there is an approximately flat background. This background represents uncorrelated particles triggering the TDC start and stop, which is also why negative ToF values appear. The gamma-flash has been shifted to be centered at 3.8 ns, the time it takes light to travel from the source to the detector. The width of the gamma-flash is primarily due to the time resolution of the detectors. This depends on where in the detector volume the gamma-ray interacts. Secondary effects include signal attenuation in the cables, which might affect PS and thus rise time. This may in turn make the CFD less effective and may cause loss in the time resolution. Furthermore, the final digitization by the TDCs may cause some loss of resolution. Differences in flight path between gamma-rays hitting the center of the NE213 detector and those that hit near the edge will be less than 1 cm, so this will not give rise to a substantial time spread. The neutron bump has more energetic

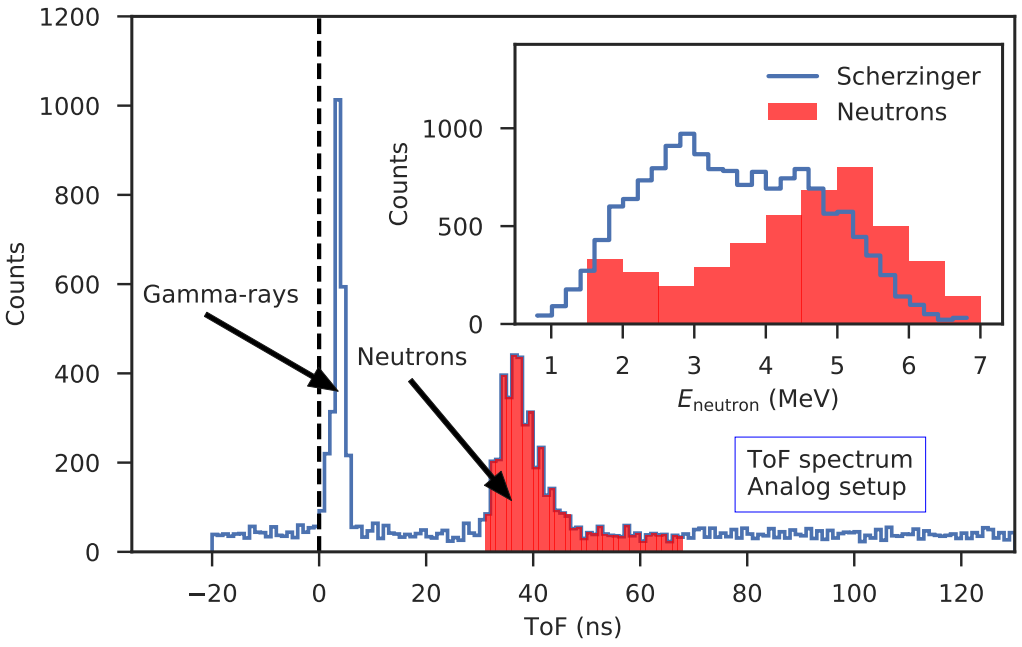

Figure 3.3: ToF spectrum, analog setup. The x-axis denotes the ToF from source to NE213 detector. The neutron and gamma-ray peaks are indicated with arrows. The coincidences highlighted in red have been converted to neutron kinetic energies and are shown in the upper right insert.

neutrons at lower ToF values and less energetic neutrons at higher ToF values. Since the distance from the source to the detector is known, it is possible to convert the neutron

ToF into neutron kinetic energy. A range of 1.5−7 MeV was chosen. This corresponds to a time interval of 31−68 ns. The coincidences falling in this time interval have been highlighted in red in Fig. 3.3 and the corresponding energies are shown in the insert. The spectrum obtained by Scherzinger [7] (recall Fig. 1.6) has been superimposed. This spectrum has been normalized to produce the best qualitative agreement possible. The Scherzinger spectrum was measured with the same source but a different and smaller NE213 detector. That detector had only ∼10% of the scintillation volume of the one used here and was cylindrical. Low-energy neutrons are clearly missing from the current data set, likely because a too large amplitude threshold has been applied. It also appears that the neutron-energy spectrum acquired by the analog setup is shifted to the right by roughly half an MeV. Below 2.5 MeV, the count rate in Fig. 3.3 increases. This is simply an effect of the last ∼20 ns primarily consisting of background.

3.2.2 Pulse-Shape Discrimination

Neutrons and gamma-rays were discriminated using the PS parameter given in Eq. 1.4. The parameters a=120 QDC channels and b=0 QDC channels were found to linearize PS as a function of energy when gate lengths of 500 ns and 60 ns were used for the LG and SG integrations respectively. PS is shown as a function of deposited energy in Fig. 3.4. Pulses in the upper band (labeled neutrons) have a large amount of charge in the tail of the scintillation pulse. Pulses in the lower band (labeled gamma-rays) have a smaller amount charge in the tail of the scintillation pulse. This is confirmed by the presence of the Compton edges corresponding to 2.23 MeV and 4.44 MeV gamma-rays in the lower band. The amplitude threshold of 94.6 mV gives rise to the sloping energy threshold highlighted with a red line in the figure. This is because pulses with higher PS have more charge in the tail, so given two pulses of equal amplitude, the one with larger PS will carry more charge.

The optimal PS-cut value of 0.259 was found by plotting a PS histogram and fitting Gaussian functions to the neutron and gamma-ray distributions, see Fig. 3.5. The quality of separation between the two distributions may be expressed as a Figure of Merit, FoM, defined in terms of the centers, C, of the Gaussian functions and their full width at half maximum, W:

$$\mathrm{FoM} = \frac{C_n - C_\gamma}{W_n + W_\gamma} \tag{3.1}$$

Figure 3.5 shows histograms of the PS parameter along with the Gaussian fits used to calculate the FoM. The corresponding parameters are listed in Table 3.2. The resulting integrated FoM was 0.58, but was found to be highly energy-threshold dependent.

The neutron and gamma-ray distributions overlap at low deposited energies. Consequently, the PSD cut can result in misclassification. Orthogonal ToF information on particle species can be used to quantify the extent of this misclassification. Figure 3.6 shows PS plotted as a function of ToF, with neutron and gamma-ray distributions highlighted. These distributions are not cleanly separated by the applied PSD cut. A significant amount of both neutrons and gamma-rays are mislabeled. Often the start and stop

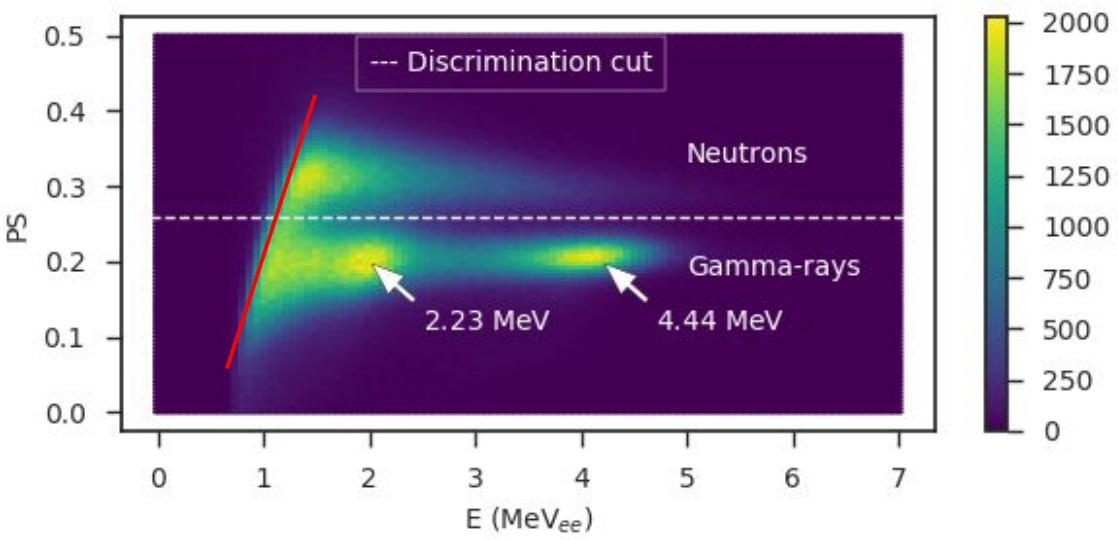

Figure 3.4: Analog PS spectrum as a function of deposited energy. The dashed white line indicates the PSD cut. Structures due to the 2.23 MeV and 4.44 MeV gamma-rays are indicated. The red line indicates the amplitude threshold.

signal will be due to uncorrelated particles, rather than the previously discussed $n\gamma$ and $\gamma\gamma$ pairs. These events are expected to form a flat background in the ToF spectrum due to low rates. This may be seen in Fig. 3.3 at times longer than 50 ns. Since the events still represent either neutrons or gamma-rays (ignoring the occasional muon), one would expect them to be clearly separated into two bands in Fig. 3.6. This is not the case.

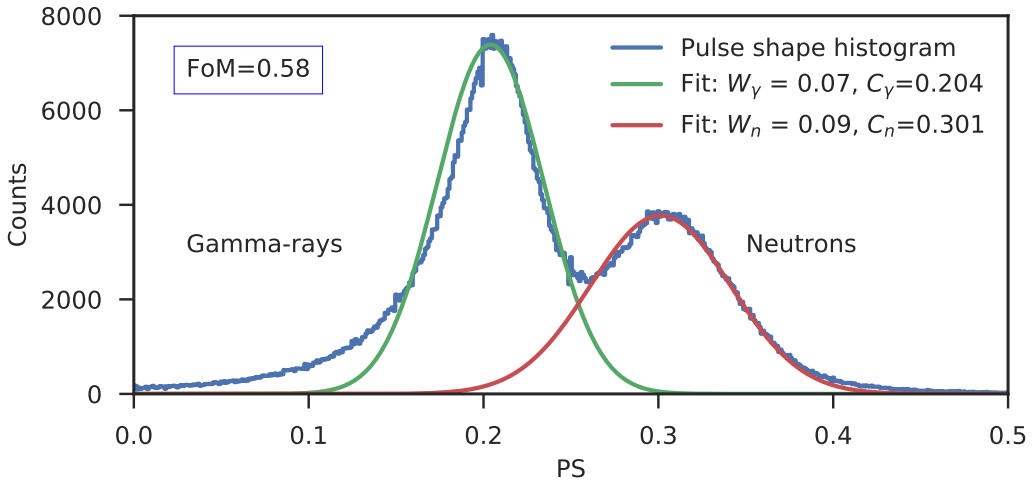

Figure 3.5: PS FoM for the analog setup.

FoM	Cut	W_γ	C_γ	W_n	C_n
0.58	0.259	0.07	0.204	0.09	0.301

Table 3.2: CC FoM parameters for the analog setup.

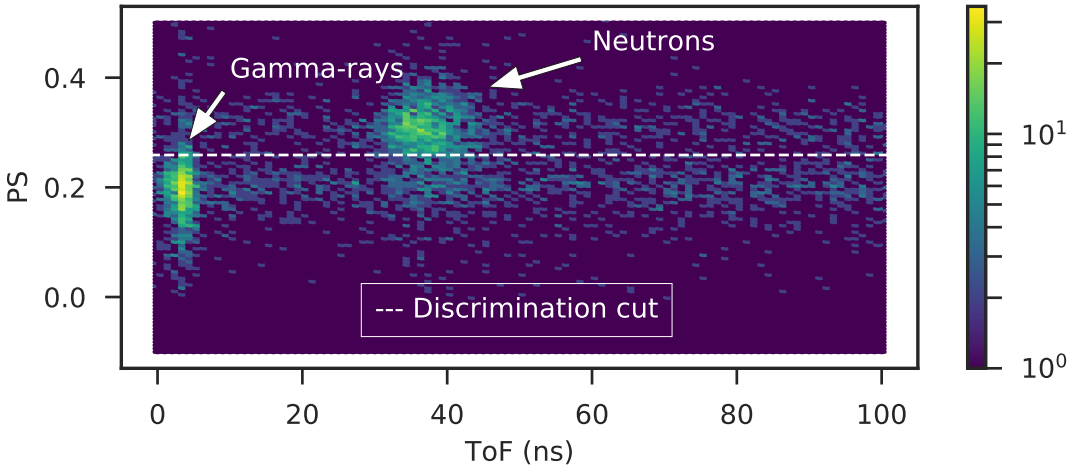

Figure 3.6: PS vs. ToF for the analog setup. The dashed white line indicates the PSD cut. Note the logarithmic z-axis.

3.3 Digital Setup

3.3.1 Neutron Tagging

Fig. 3.7 shows the ToF spectrum acquired with the digital setup. No additional threshold cuts or normalizations have been applied. Gamma-ray and neutron peaks are indicated. Random coincidences form a flat background. The width of the gamma-flash is again due to the intrinsic time resolution of the detectors. A secondary effect may be the digitization of the pulse. Limited resolution and sampling rate might cause the CFD algorithm to trigger slightly too soon or too late. The red-shaded flight times in the neutron peak have been used to generate the energy spectrum shown in the insert of Fig. 3.7. The same time (31−68 ns) and energy (1.5−7 MeV) ranges used for the analog setup have been used here. The spectrum has far more events at lower energies than the corresponding spectrum for the analog setup, recall Fig. 3.3. This is because the digital setup had a lower amplitude threshold than the analog setup. Thus, neutrons with less energy, which generally produce current pulses of lower amplitude in the detector, may be recorded by the digital setup. The energy spectrum looks qualitatively very similar to the superimposed reference spectrum of Scherzinger. However, the low-energy peak is located at slightly higher energy. Scherzinger might have applied an even lower threshold.

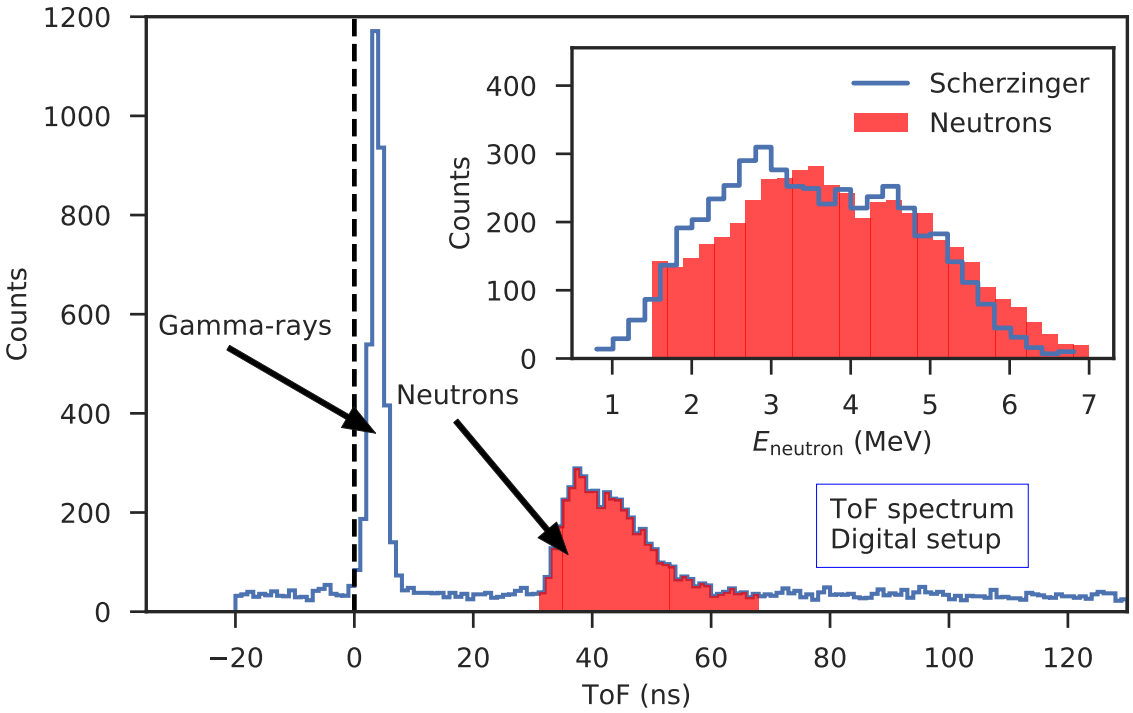

Figure 3.7: ToF spectrum, digital setup. The x-axis denotes the ToF from source to NE213 detector. The neutron and gamma-ray peaks have been indicated with arrows. The coincidences highlighted in red have been converted to neutron kinetic energies and are shown in the upper right insert.

3.3.2 Pulse-shape Discrimination

As with the analog setup, 500 ns and 60 ns LG and SG integration windows were used to perform PSD. To linearize the bands, the parameters a and b from Eq. 1.4 were chosen as a=287 and b=120 (in uncalibrated digital-integration channels). The resulting PSD spectrum is shown in Fig. 3.8a. The Compton edges corresponding to 2.23 MeV and 4.44 MeV gamma-rays are indicated with arrows. A large number of low-energy gamma-rays appear at the bottom left hand corner of the plot due to the lower threshold. A cut at PS=0.222 separates the neutron and gamma-ray bands. Again, the two distributions overlap at lower deposited energies.

The CNN described in Sec. 2.3 was also applied to the digitized waveforms. The network was trained to assign a value y between 0 (gamma-ray) and 1 (neutron) to each signal. The result is shown in Fig. 3.8b as a function of deposited energy. As for the CC method, the upper distribution corresponds to neutrons and the lower distribution to gamma-rays. The two bands are separated by a PSD cut at 0.5. To highlight that the distributions overlap slightly at lower energies, the z-axis has been strongly suppressed. The CNN, trained on events from the two ToF peaks, allows for much cleaner separation

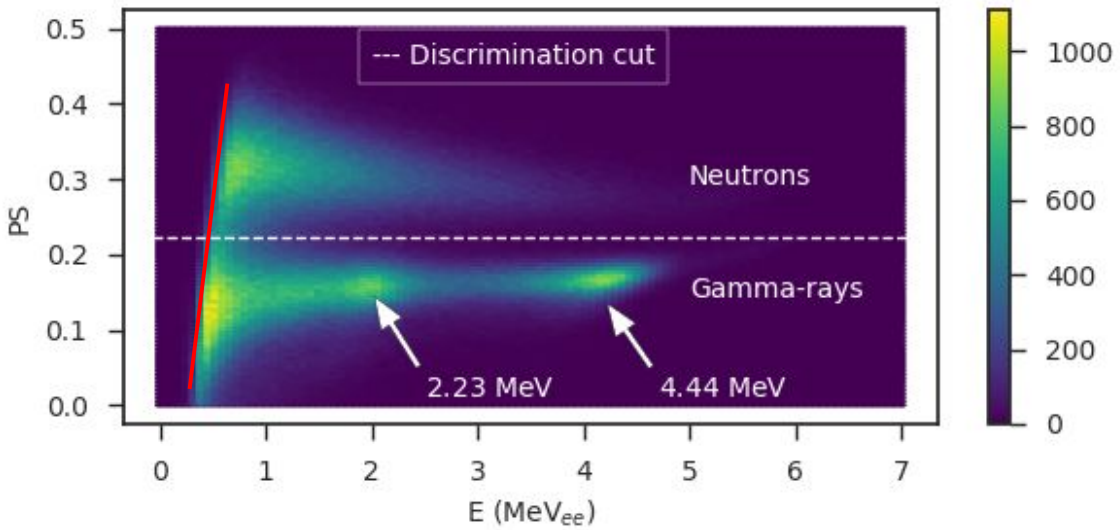

(a)

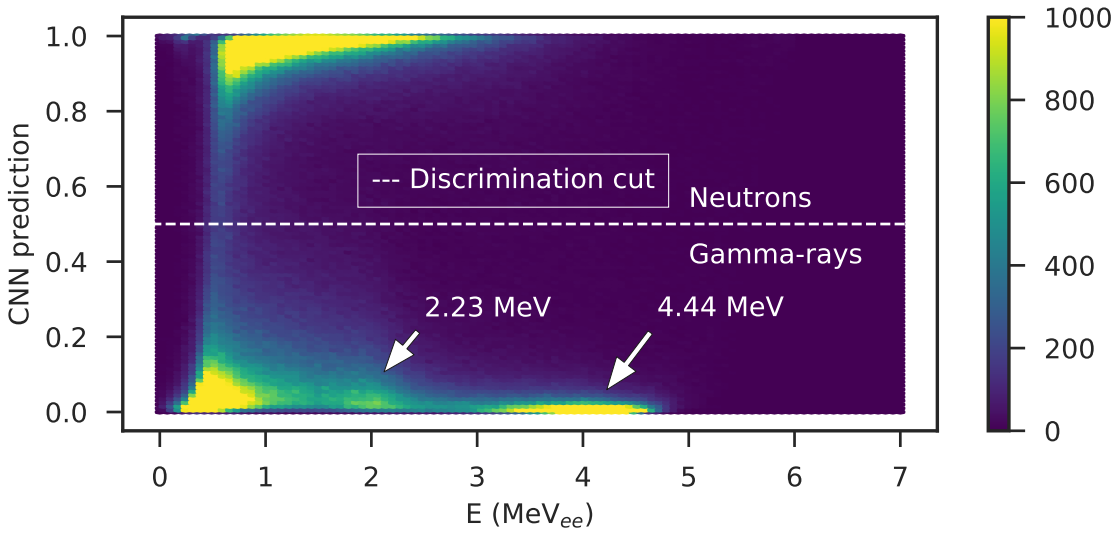

(b)

Figure 3.8: Digital PS discrimination as a function of deposited energy. The dashed white lines indicate PSD cuts. Structures due to the 2.23 MeV and 4.44 MeV gamma-rays are indicated. Top panel: CC method. Amplitude threshold is indicated with a red line. Bottom panel: CNN method.

between particle species, so that the exact location of the PSD cut is much less critical than in either of the CC implementations.

As for the analog setup, a FoM was calculated based on Gaussian fits to the PS distribution, see Fig. 3.9. The FoM parameters are summarized in Table 3.3. With an integrated FoM of 0.78, the digital implementation of the CC method provides better results than the analog implementation.

FoM	Cut	W_γ	C_γ	W_n	C_n
0.78	0.222	0.07	0.160	0.11	0.300

Table 3.3: CC FoM parameters for the digital setup.

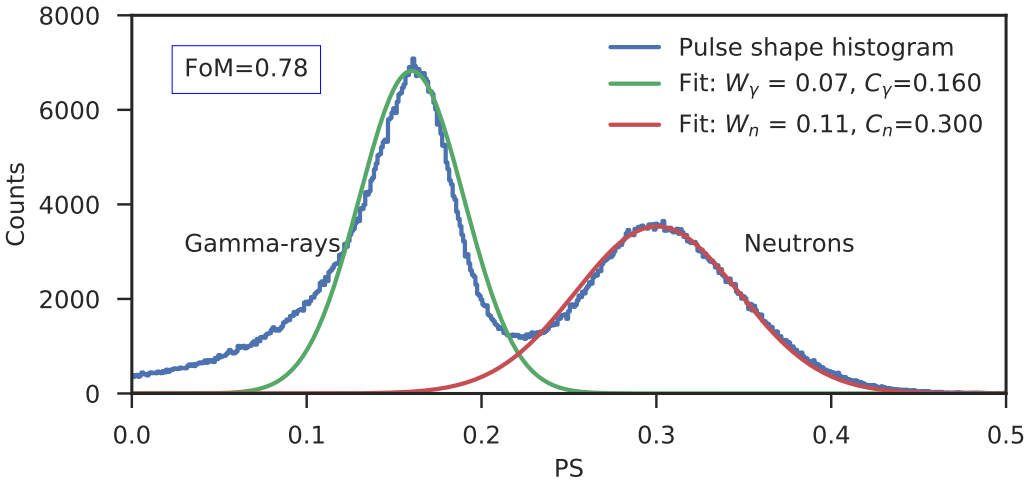

Figure 3.9: PS FoM for the digital setup.

In Fig. 3.10, the digital CC and CNN predictions are shown as functions of ToF. Figure 3.10a shows the narrow gamma-ray distribution and the wider neutron distribution as separated by the digital CC method. The neutron and gamma-ray background forms two slightly separated bands near prediction values 0.3 and 0.15 respectively. The two distributions overlap somewhat. In Fig. 3.10b, it can be seen that the CNN method provides a much better separation, although gamma-ray and neutron distributions still overlap slightly near prediction value 0.5. The distribution of random coincidences separates into a gamma-ray band near prediction value 0 and a neutron band near 1.

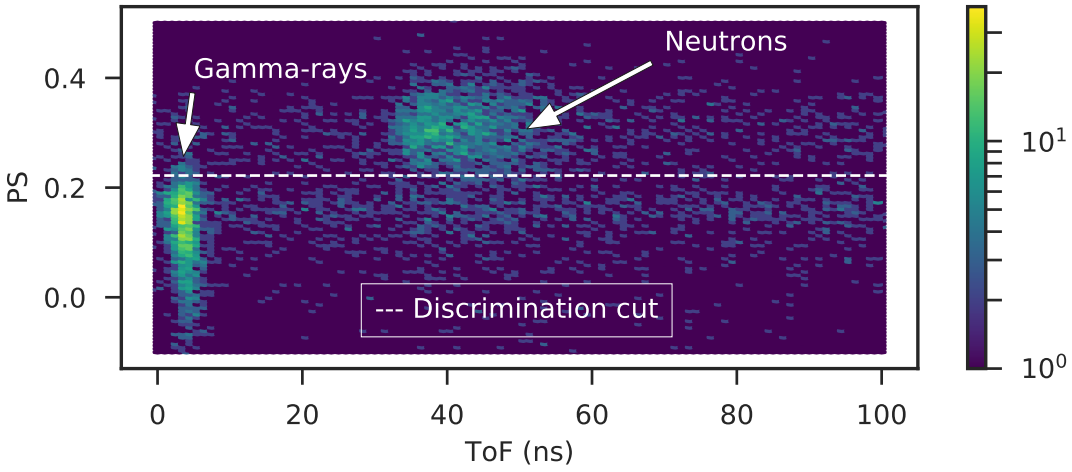

(a)

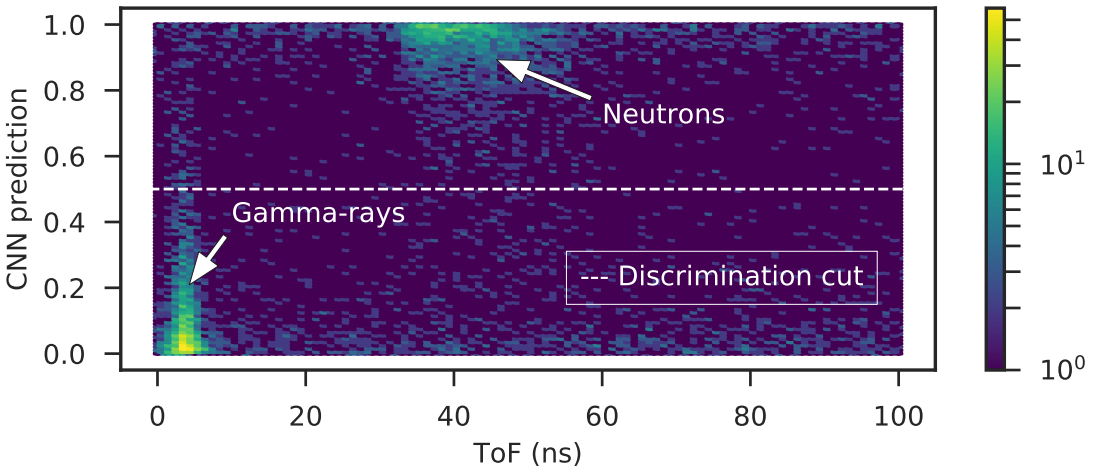

(b)

Figure 3.10: PS vs. ToF for the digital setup. The dashed white line indicates the PSD cut. Note the logarithmic z-axis. Top panel: CC method. Bottom panel: CNN method.

3.4 Misclassification

Another way to compare the performance of the PSD methods is by estimating the misclassification. This can be done by evaluating the ToF spectrum in three different regions and comparing the relative number of neutron and gamma-ray labeled events. It is anticipated that the number of gamma-rays identified in a background region containing only random coincidences should be the same as the number of gamma-rays identified in a chosen neighborhood of the neutron time-of-flight peak after scaling to the widths of the regions. Likewise, the number of neutrons identified at the gamma-flash should correspond to the neutron-background expectation. The misclassification of gamma-rays and neutrons, M_γ and M_n respectively, can then be expressed as

$$M_\gamma(R_\gamma) = \frac{N_n(R_\gamma) - \langle N_n(R_\gamma)\rangle}{N_{\text{total}}(R_\gamma) - \langle N_n(R_\gamma)\rangle} \tag{3.2}$$

$$M_n(R_n) = \frac{N_\gamma(R_n) - \langle N_\gamma(R_n)\rangle}{N_{\text{total}}(R_n) - \langle N_\gamma(R_n)\rangle}, \tag{3.3}$$

where N_n and N_γ are the number of neutrons and gamma-rays identified in region R and N_{total} is the sum of N_n and N_γ. $\langle N_n\rangle$ and $\langle N_\gamma\rangle$ are the expected numbers of neutrons and gamma-rays found by scaling the background rates to the width of R. This definition of misclassification relies on the assumption that the choice of limits for each of the three regions does not seriously impact the results. The neutron peak neighborhood was set to match the range of neutron energies $1.5-7\,\text{MeV}$ corresponding to $31-68\,\text{ns}$ and the gamma-flash neighborhood was selected as $5\,\text{ns}$ on either side of the gamma-flash center. It was found that as long as the peaks were contained in these regions the misclassifications changed by at most $\pm 0.5\%$ for the digital setup and at most $\pm 1\%$ for the analog setup.

Figure 3.11 shows the ToF spectrum obtained with the analog setup filtered according to the CC method, as well as the ToF spectrum obtained from the digital setup filtered according to the CC and CNN methods. For each PSD implementation, gamma-ray labeled events are blue, neutron labeled events are red and their intersection purple. Ideally, the intersection of the distributions should be flat. However, if there is some systematic misclassification, then the intersection will rise above the flat background level in the ToF spectrum. This may be used to quantify the misclassification of a given PSD implementation. For the analog setup, a high degree of contamination is evident in the form of the two purple bumps coinciding with the neutron and gamma-ray peaks. This gives an estimated misclassification of 16% for neutrons and 12% for gamma-rays. The digital setup provides less misclassification with the CC method, at 12% for neutrons and 3% for gamma-rays. The much higher misclassification for neutrons implies that the method is biased towards gamma-rays. The CNN approach reaches the best results with a gamma-ray misclassification of 4% and a neutron misclassification of 5%. With a misclassification of nearly the same amount for both neutrons and gamma-rays, the CNN method does not appear to have a strong bias towards either particle species. The neutron background is found to be nearly the same by the analog and digital CC methods,

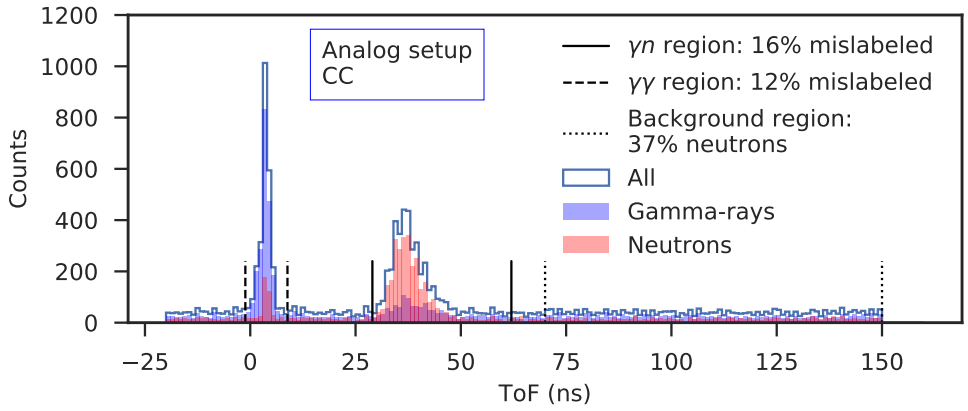

(a) PSD cut at PS = 0.259.

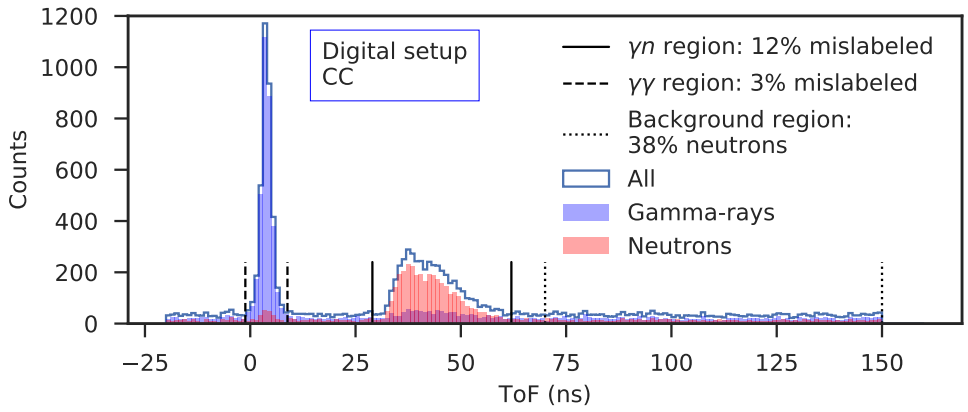

(b) PSD cut at PS=0.222.

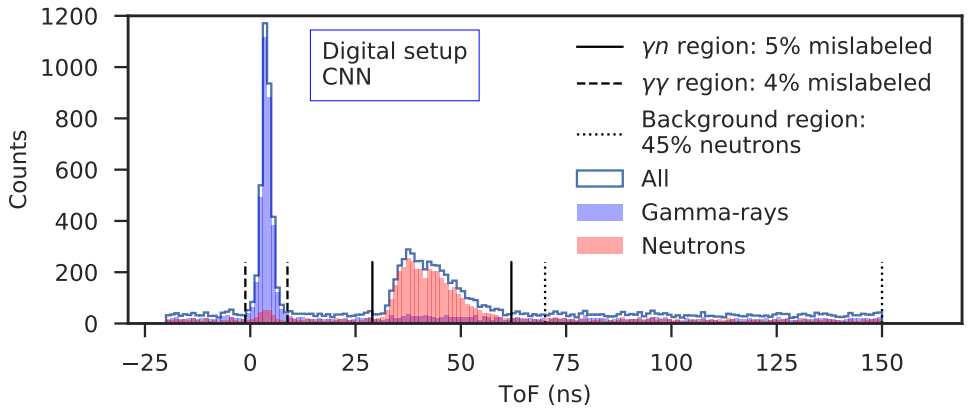

(c) PSD cut at prediction = 0.5.

Figure 3.11: Filtered ToF spectra for misclassification studies.

at 37% and 38% respectively. The CNN method finds a significantly higher background of neutron events at 45%. This together with the high misclassification rates for the CC methods hints at them being biased towards gamma-rays. The results from all three PSD implementations are summarized in Table 3.4.

	γn-region (% misclassified)	$\gamma\gamma$-region (% misclassified)	Background region (% neutrons)
CC Analog	16	12	37
CC Digital	12	3	38
CNN Digital	5	4	45

Table 3.4: Overview of PSD misclassification studies.

3.5 Neutron Kinetic Energy and Energy Deposition

Figure 3.12 shows energy deposition in the NE213 detector as a function of ToF measured with the digital setup. The least energetic neutrons (ToF $\sim$60 ns) have a smaller spread in deposited energy, whereas the faster neutrons (ToF $\sim$35 ns) have a much larger spread. This may be explained by the fact that in the NE213 detector, the neutron scatters primarily from ^{1}H nuclei. Thus, by Eq. 1.3, the neutron may deposit up to its entire kinetic energy in a single scatter. A low-energy neutron simply has less energy to transfer, resulting in the smaller spread in deposited energy.

The scintillation-light output produced by an NE213 detector is given by [23]:

$$\mathrm{E_{deposited}} = C\left(0.83\cdot \mathrm{E_p} - 2.82\cdot\left(1 - e^{(-0.25\cdot \mathrm{E_p^{0.93}})}\right)\right), \tag{3.4}$$

where $E_{\mathrm{deposited}}$ and E_{p} is the energy deposited in the detector in $\mathrm{MeV_{ee}}$ and the kinetic energy of the proton producing the light in MeV, respectively. The parameter C is a scaling parameter which allows for such effects as scintillator aging and batch-to-batch variation in scintillator quality. As a first approximation the kinetic energy found from the ToF may be used in place of proton energy. This is not a bad approximation when using a large detector where the neutron can undergo multiple scattering transferring most of its energy to recoiling protons. In Fig. 3.13 (top panel), the deposited energy is shown for three intervals of kinetic energy of the neutron. Clearly, both the positions and the widths of the peaks vary. The positions of the deposited-energy distributions are plotted as a function of neutron kinetic energy in the bottom panel. Uncertainties correspond to the fitted widths. By fitting Eq. 3.4 to these data, the value of C was found to be 0.62. This means that the NE213 scintillator is performing at 62% of the benchmark. Note that Rofors measured this parameter for this detector in 2016 and

found it to be 86% [13]. The detector thus seems to be degrading at a rate of ∼8% per year. This is likely because the boroscilicate glass/photocathode interface needs new optical grease.

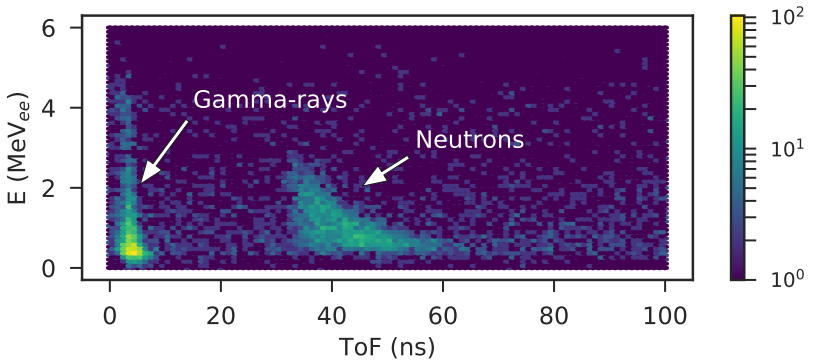

Figure 3.12: ToF plotted against energy deposition for the digital setup.

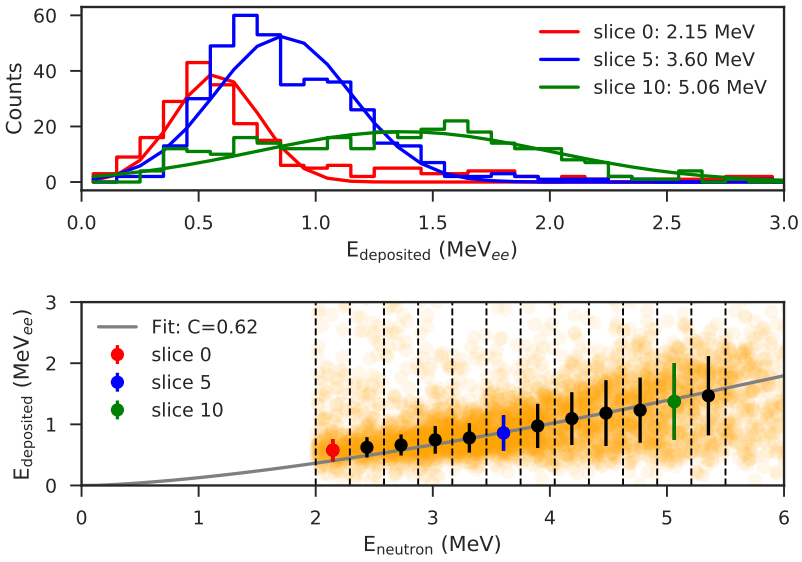

Figure 3.13: Deposited energy and neutron kinetic energy. Top: Gaussian fits to deposited energies for selected slices of neutron kinetic energy. Bottom panel: deposited energy as a function of neutron kinetic energy, along with the fitted function.

Chapter 4

Closing Remarks

4.1 Summary

The advantages of performing neutron-tagging measurements using a waveform digitizer were explored. An existing analog setup consisting of modular crate electronics at the STF at the Division of Nuclear Physics in Lund, Sweden was digitally replicated. Neutrons were detected using an organic liquid-scintillator detector while the corresponding 4.44 MeV gamma-rays were detected using inorganic scintillation crystals. The performance of the digitizer-based setup was compared to that of the modular analog setup in terms of neutron and gamma-ray PSD and ToF. The results obtained using the digitizer-based approach are superior to those obtained using the modular analog electronics approach in all aspects. The digitizer-based approach was then succesfully employed to both distinguish between neutrons and gamma-rays via a CNN and to relate neutron deposition-energy to neutron kinetic energy via ToF.

4.2 Conclusions

In conclusion, the digital setup significantly outperformed the analog setup in terms of CC PSD capabilities. The digital setup also facilitated a CNN-based PSD approach, which outperformed both the analog and the digital CC implementations. The measurements from the analog setup were hampered by the use of a too-high amplitude threshold. This is a classic pitfall associated with analog electronics. Unlike the digitizer approach, choices of thresholds and gate lengths for the analog setup can not be undone after the dataset has been acquired. A limiting factor with the digital setup is the dynamic range, which needs to be carefully allocated. Likewise the data transfer needs to be partitioned into blocks to minimize deadtime. Indeed, the dynamic range of the digitizer was not optimized for the measurements performed here, resulting in clipping for high energy gamma-rays. Additionally, ToF information was used to relate the neutron kinetic energy to its deposited energy. It was found that the NE213 detector had degraded with time.

4.3 Outlook

Much has been learned about the two DAQs which can be used to make them perform even better in future experiments. It is clear that the analog setup is pedagogically superior to the digital setup, but it requires careful optimization before use. The digital setup requires careful allocation of the dynamic range and of the data-transfer rate. Finally the software WaveDump felt primitive and could likely be improved upon by custom software fine-tuned to the task at hand. Indeed, this is underway. There are ways to optimize both digital PSD implementations. The digital CC method will likely benefit from different integration-gate lengths. Further, the possibility of using shielding to obtain separate gamma-ray and neutron data sets for CNN training needs to be explored. Additionally other PSD methods such as Fourier transform-based PSD should be explored. The future clearly lies with the digitizer approach.

Bibliography

[1] Brookhaven National Laboratory National Nuclear Data Center. Nudat (nuclear structure and decay data), March 18, 2008 2008.

[2] K. S. Krane. *INTRODUCTORY NUCLEAR PHYSICS*. 1988.

[3] W. R. Leo. *Techniques for Nuclear and Particle Physics Experiments: A How to Approach*. 1987. ISBN 9783540572800.

[4] S. Tavernier. *Experimental Techniques in Nuclear and Particle Physics*. Springer Berlin Heidelberg, 2010. ISBN 9783642008290. URL `https://books.google.se/books?id=C1GT__RkewUC`.

[5] J. Scherzinger, J.R.M. Annand, G. Davatz, K.G. Fissum, U. Gendotti, R. Hall-Wilton, E. Håkansson, R. Jebali, K. Kanaki, M. Lundin, B. Nilsson, A. Rosborge, and H. Svensson. Tagging fast neutrons from an 241am/9be source. *Applied Radiation and Isotopes*, 98:74 – 79, 2015. ISSN 0969-8043. doi: https://doi.org/10.1016/j.apradiso.2015.01.003. URL `http://www.sciencedirect.com/science/article/pii/S0969804315000044`.

[6] Nicholai Mauritzsson. Design, construction and characterization of a portable fast-neutron detector, 2017. Student Paper.

[7] Julius Scherzinger. *Neutron Irradiation Techniques*. PhD thesis, Lund University, 2016.

[8] F. Messi et al. The neutron tagging facility at Lund University. 2017.

[9] Julius Scherzinger, Ramsey Al Jebali, John Annand, Kevin Fissum, Richard Hall-Wilton, Sharareh Koufigar, Nicholai Mauritzson, Francesco Messi, Hanno Perrey, and Emil Rofors. A comparison of untagged gamma-ray and tagged-neutron yields from ^{241}AmBe and ^{238}PuBe sources. *Appl. Radiat. Isot.*, 127:98–102, 2017. doi: 10.1016/j.apradiso.2017.05.014.

[10] Eljen Technology. Neutron/gamma psd ej-301, ej-309. URL `https://eljentechnology.com/products/liquid-scintillators/ej-301-ej-309`. Retrieved: April 23rd 2019.

[11] Johan Sjögren. *Construction and initial testing of a neutron detector prototype*. Lund University, 2010.

[12] Scionix. Yap:ce detectors for fast x-ray spectroscopy. URL `https://scionix.nl/wp-content/uploads/2017/07/YAP-Ce-scintillators.pdf`. Retrieved: May 1rst 2019.

[13] Emil Rofors. Fast photoneutron detection, 2016. Student Paper.

[14] CAEN. *Technical Information Manual, MOD. V775 series, MOD. V775 N series*. CAEN, 2012.

[15] Björn Nilsson. *High-Resolution Measurements of the ^{4}He(γ,n) Reaction in the Giant Resonance Region*. Lund University, 2003.

[16] CAEN. *User Manual, UM3350 V1751/VX1751, 4/8 Channels 10bit 2/1 GS/s Digitizer*. CAEN, 2017.

[17] A. Pini, G. Tate, and O. Rovini. An introduction to modular waveform digitizers. URL `https://spectrum-instrumentation.com/sites/default/files/download/an_waveformdigitizers_introduction.pdf`.

[18] CAEN. Wavedump, 2018. URL `https://www.caen.it/products/caen-wavedump/`. version 3.8.1.

[19] Dask Development Team. *Dask: Library for dynamic task scheduling*, 2016. URL `https://dask.org`.

[20] Wes McKinney. Data structures for statistical computing in python. In Stéfan van der Walt and Jarrod Millman, editors, *Proceedings of the 9th Python in Science Conference*, pages 51 – 56, 2010.

[21] J. Griffiths, S. Kleinegesse, D. Saunders, R. Taylor, and A. Vacheret. Pulse Shape Discrimination and Exploration of Scintillation Signals Using Convolutional Neural Networks. 2018.

[22] François Chollet et al. Keras. `https://keras.io`, 2015.

[23] R.A. Cecil, B.D. Anderson, and R. Madey. Improved predections of neutron detection efficiency for hydrocarbon scintillators from 1 MeV to about 300 MeV. *Nuclear Instruments and Methods*, 161(3):439 – 447, 1979. ISSN 0029-554X. doi: https://doi.org/10.1016/0029-554X(79)90417-8. URL `http://www.sciencedirect.com/science/article/pii/0029554X79904178`.